

University of Nevada, Reno

**DEVELOPMENT OF THE MAGNETIC SHIELDING AND ROTATIONAL
STABILITY APPARATUS FOR USE IN THE ARIADNE PROJECT**

A Thesis Submitted in Partial Fulfillment
of the Requirements for the Degree of Master of Science in
Physics

by

Jordan Dargert

Dr. Andrew Geraci / Thesis Advisor

May 2018

© 2018 Jordan Dargert
ALL RIGHTS RESERVED

**UNIVERSITY
OF NEVADA
RENO**

THE GRADUATE SCHOOL

We recommend that the thesis prepared
under our supervision by

JORDAN DARGERT

entitled

**DEVELOPMENT OF THE MAGNETIC SHIELDING AND ROTATIONAL
STABILITY APPARATUS FOR USE IN THE ARIADNE PROJECT**

be accepted in partial fulfillment of the
requirements for the degree of

MASTER OF SCIENCE

Andrew Geraci, Ph.D. – Advisor

Jonathan Weinstein, Ph.D. – Committee Member

Dev Chidambaram, Ph.D. – Graduate School Representative

David W. Zeh, Ph.D. – Dean, Graduate School

May 2018

ABSTRACT

The QCD axion is a particle that is postulated to solve the Strong-CP problem, but also could account for all of the Dark Matter currently being observed in the Universe. Our group is involved in developing an experiment with the goal of detecting the QCD Axion. The Axion Resonant InterAction DetectioN Experiment (ARIADNE) aims to accomplish this goal by using a resonantly enhanced technique to test for new spin-dependent forces, which are short range in nature. Thus the sample mass is modulated on resonance near a sample of Helium-3 needs to be highly stable. The goal is to measure a spin-mass interaction produced by the axion particle. The experiment employs a rotary stage mechanism to modulate the interaction, which requires rotational speed stability and low vibration. Also, superconducting magnetic shielding is required to screen the sample from ordinary magnetic field noise. The purpose of this thesis is to develop the rotation stability stage and magnetic shielding. In doing so, we were able to develop and test the efficacy of the interferometer system that monitors the motion of the mass, and the ability to produce a drive shaft with a high degree of straightness. The shielding factor of the superconducting shield was modeled and tested for specific geometries; we did demonstrate that a shielding factor of 10^8 is achievable.

ACKNOWLEDGEMENTS

I would like to take a moment to thank all of the collaborators of ARIADNE such as Asimina Arvanitaki, Aharon Kapitulnik, Eli Levenson-Falk, Sam Mumford, Josh Long, Chen-Yu Liu, Mike Snow, Erick Smith, Justin Shortino, Mofan Zhang, Andrew Rusch, Yannis Semertzdis, Yun Shin, and Yong-Ho Lee. Along with the collaborating institutions: University of Nevada Reno, University of Indiana, Stanford, Perimeter Institute, CAPP, KRISS, and Northwestern University.

Additionally I would like to thank Dr. Andrew Geraci for assistance, guidance, and wisdom, but for also allowing me to be a part of this ambitious project. I want to thank the research group: Chloe Lohmeyer, Harry Fosbinder-Elkins, Mindy Harkness, Mark Cunningham, Cris Montoya, Gambhir Ranjit, and many others for all their assistance, guidance, and friendship over the years.

TABLE OF CONTENTS

Abstract	i
Acknowledgements	ii
Table of Contents	iii
List of Tables	iv
List of Figures	v
1 Introduction	1
1.1 Peccei Quinn Axions	1
1.2 Spin-Dependent Forces	5
1.3 ARIADNE Experiment	7
1.3.1 Spinning Mass	8
1.3.2 Sample Block	10
2 Design of chamber	13
2.1 Bottom Plate	13
2.2 Middle Plate	14
2.3 Upper Section and Outer Dewar	16
2.4 Design Final Remarks	18
3 Magnetic Shielding Calculations	19
3.1 Sample Geometry	19
3.2 Method of Images and the Meissner Effect	19
3.2.1 Higher Order Images	23
3.3 Magnetic Field Correction	25
3.3.1 D Shaped Helmholtz Bias Field	28
4 Block Design	30
4.1 Magnetic Gradient Modeling	30
4.2 Spheroid Machining and Block Design	37
5 Rotational Stability Test Chamber	40
5.1 Chamber Design	40
5.1.1 Aerotech Motor Configuration	42
5.1.2 Shinsei Motor Configuration	43
5.2 Motor Rotational Speed Stability	43
5.3 Test Mass Assembly	46
5.4 Interferometer	50
5.5 Results	53
6 Conclusions and Future Work	57
Bibliography	58

LIST OF TABLES

1.1	List of basic axion properties	2
5.1	Glass Rod Dimension Data in inches	47
5.2	Titanium Rod Dimension Data in inches	48

LIST OF FIGURES

1.1	Here depicted are two separate fermions separated by a distance 'r'. The axion provides an interaction between the mass 'm' of one fermion and the spin ' σ ' of another as shown in equation 1.1.	3
1.2	Current experimental bounds on the QCD axion mass range. Most experiments explore the ranges they are listed next to. ARIADNE aims to look at the green area where no current experiments exist [6].	4
1.3	As with the depiction in Figure 1.1 the effective magnetic field produced by the oscillating mass interacts with the spin of the fermion in the external bias magnetic field.	7
1.4	Setup: a sprocket-shaped source mass is rotated so its "teeth" pass near a laser-polarized ^3He NMR sample at its resonant frequency, producing a time-varying "fictitious" magnetic field via the axion potential. The resulting induced transverse magnetization is read out using a SQUID magnetometer. This distance between the rotating sprocket and He sample is kept within $\approx 200 \mu\text{m}$ to search for short-range axion-mediated forces [12]. Not to scale.	8
1.5	Example Tungsten source mass	10
1.6	Axion parameter space as function of the axion force range and the coupling. The red band indicates the limits as defined by the transverse magnetization noise, a long T_2 time achieved by an integration time of 10^6 . The solid blue line indicates the projected reached based on potential future improvements. The bounds and current constraints are also shown [13].	11
2.1	Bottom plate assembly.	13
2.2	Middle plate configuration.	15
2.3	a) Total chamber with transparent dewar, b) total chamber with dewar and can removed.	17
3.1	Example depiction of a top down cross sectional view of the sample vessel and the spinning mass.	20
3.2	Meissner image generation example. Images show the relationship between the magnetic field B and the magnetization m.	22
3.3	Example of what the magnetic fields look like inside the sample spheroid when in the presence of a Meissner image spheroid with a nuclear spin density of $2 \times 10^{21} \text{ spins/cc}$ and a DC bias of $\approx 3 \mu\text{T}$	23
3.4	(left) The field cancellation method has the goal of canceling the field from the image spheroid by generating a opposing dipole field. (right) Gradient cancellation seeks to accomplish the same goal but by using a complimentary dipole field to minimize the variance from the norm.	27

3.5	Example image of the D shaped Helmholtz coil with its associated image coil.	28
4.1	Schematic for the quartz sample block. This provides a scheme for how each component will be fabricated onto their individual portions of quartz, but also shows how they fit together. Once glued together, the block will be coated in Niobium.	31
4.2	a) shows a solid tube of Nb used to measure the shielding factor. The tube was 200mm in length, 23mm ID, and the Nb thickness was 1mm. Below is the SQUID magnetometer used in measurement. b) Shows the COMSOL model of a the same solid Nb tube in an axial magnetic field to be used for comparison.	33
4.3	Plots of the magnetic field along the axis of the tube emerging from the superconducting shield, where the length of the superconducting portion of the central wire is varied from no superconducting wire, to one that extends to a point 10mm from the end of the tube, to one that extends to the end of the tube [12].	34
4.4	The line plots show the axial magnetic field penetration. Each line shows a different tube length, thus illustrating the effectiveness of different tube lengths without the presence of a central wire [12]. . .	36
4.5	a) Plot showing the shielding factor when the Palladium junction is in place. b) Design of the SQUID loop to be implemented into ARIADNE.	37
4.6	Machined spheroid half section example with $5\mu\text{m}$ steps. The Coloration is due to dyes that were used so a photo could be taken. . . .	38
4.7	Profilometer data after applying failed acid etch to smooth steps. . .	38
5.1	SolidWorks models of a) Aerotech chamber configuration with appropriate clamp design, b) chamber with top can attached, c) Fukoku motor configuration with appropriate clamp design.	41
5.2	Spin speed stability provided by the Aerotech built-in optical encoder performed under no load and in air. VelErr is the velocity error signal, VelFbk is the feedback signal, and VelCmd is the velocity command signal.	44
5.3	Spin speed stability provided by a basic photo detector. The spikes in the data represent each time the HeNe laser passes the detector. All of the base line noise is due to ambient light in the room at the time of measurement.	45
5.4	a) Brass test mass with timing grooves and glass rod inserted via hot plate and allowed to cool. The brass contracts to the point of holding on to the rod. b) Example Tungsten mass.	46

5.5	Shows a Titanium rod with the center bearing being pressed into place via liquid Nitrogen. The rod is dipped in liquid Nitrogen at one end to allow the Titanium to cool while isolating the bearing as much as possible.	49
5.6	a) Shows a Titanium rod with both bearings fixed into place via liquid Nitrogen. b) Shows the jig made to test the TRO of each rod both with and without bearings. The jig holds the rod in the places where the bearings would be. As the rod rotates the dial reads the total deflection of the end of the rod.	50
5.7	a) Shows the modified clamp with the new bearing caps. The purpose is to allow an easy way to insert the motor assembly and hold on the the bearings. b) Shows a zoomed in model of the complete large motor assembly.	51
5.8	Example of the scheme behind the interferometer using the fiber splitter. The signal PD is how we collect the interference from the experiment and compare to the reference.	51
5.9	Signal generated by the interferometer interacting with a piezoelectric mirror.	52
5.10	Geometric example of the wobble of the spinning mass. It indicated the important variables in order to determine the wobble distance 'd' and thus the horizontal wobble 'x'.	52
5.11	Plots show a) the raw unprocessed interferometer data taken over 60s, and features all the fringes transitioned through, and b) the processed data that features a single rotation and the fringes transitioned through in a single rotation using Origin as the software. . . .	54
5.12	Photo of the bounce test arrangement of mirrors and photo-detector.	

CHAPTER 1

INTRODUCTION

1.1 Peccei Quinn Axions

There is a well-documented problem within the discipline of particle physics and in particular within Quantum Chromo Dynamics (QCD). It starts with the notion of strong interactions in the standard model. Strong interactions, which produce the strong nuclear force, are responsible for holding nuclei together. The strong force has a non-trivial vacuum structure which in turn allows CP violation. Charge conjugation refers to a transformation of a particle with its antiparticle counterpart. Furthermore, C-symmetry states that the physical laws remain unchanged under the transformation except for charge. For example, a positive coulomb force becomes a negative coulomb force, and so on. Parity inversion describes the changing of signs on one of the spatial coordinates. Which is analogous to the chirality of various molecules, referring to the right-handedness or left-handedness of a molecule. The combination of Charge symmetry and Parity inversion gives CP-symmetry, which maintains all of the same rules as before, and this rule generally follows for all forces except the weak force. This phenomenon is known as CP-violation [28]. This notion gives rise to an angle θ_{QCD} [24] currently found in the standard model. The problem is that this θ_{QCD} term should be roughly equal to one and therefore induce a much larger electric dipole moment (EDM) of the neutron. While the dipole moment of the neutron has not been measured directly, the upper bounds from experiments do place limits on θ_{QCD} in the neighborhood of 10^{-10} rad. In 1977 Roberto Peccei and Helen Quinn hypothesized a solution to the Strong CP Problem. The Strong CP problem stems from strong interactions in the

standard model [24]. Thus the solution posed by Peccei and Quinn was to propose a new particle that would relax the value of θ_{QCD} to a near zero result [24, 27, 22]. Which helps confirm what we have been experimentally observing the EDM of the neutron to be. That proposed particle is the Axion, and more specifically the QCD axion.

Table 1.1
Axion Properties

Symbol	A^0
Mass	$10^{-6} - 10^{-3} \text{ eV}$
Charge	0
Spin	0
Scalar Coupling	$6 \times 10^{-27} \left(\frac{10^9 \text{ GeV}}{f_a}\right) \leq g_s \leq 10^{-21} \left(\frac{10^9 \text{ GeV}}{f_a}\right)$
Dipole Coupling	$g_p = C_f 10^{-9} \left(\frac{m_f}{1 \text{ GeV}}\right) \left(\frac{10^9 \text{ GeV}}{f_a}\right)$

Table 1.1: List of basic axion properties

The QCD axion is a pseudo-scalar particle, which means that it behaves in a similar way to a scalar particle, but it is not invariant under CP-symmetry. So in the case of the axion, it does change sign under parity inversion. Table 1.1 shows a variety of basic properties exhibited by the axion. The couplings g_s and g_p [2] are inherently small and are directly correlated to the axion's mass, which is also small. The term C_f is a model-dependent constant [2], m_f is the mass of the fermion, and f_a is the axion decay constant which is constrained by $10^9 \text{ GeV} \leq f_a \leq 10^{17} \text{ GeV}$.

Dark Matter is a very well accepted component of the Universe, and there appears to be a large amount of it. Dark Matter doesn't interact electromagnetically like normal matter which is why it is referred to as dark. It also weakly interacts with normal matter gravitationally, which in turn makes it difficult to find and interact with [14]. The advantageous thing about axions is that they fit the general mass range of Dark Matter[2] and there is an idea of how they interact with nor-

mal matter. so that gives us a starting point to find it, but axions also help solve the strong CP problem [24]. Thus the axion is an extremely well-motivated particle to search for due to the numerous solutions it provides.

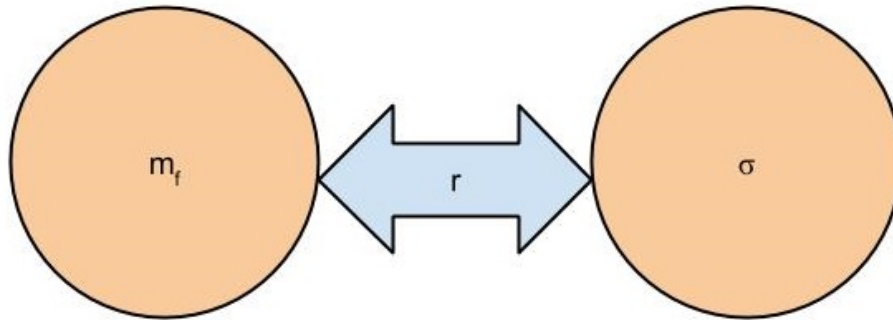


Figure 1.1: Here depicted are two separate fermions separated by a distance ' r '. The axion provides an interaction between the mass ' m ' of one fermion and the spin ' σ ' of another as shown in equation 1.1.

There are a variety of experiments looking for QCD axions and other axion-like particles. One such experiment is ADMX (Axion Dark Matter experiment) which seeks to look for axions using a resonant microwave cavity and a large superconducting magnet to convert cosmic axions into microwave photons [3]. Another is CAST (CERN Axion Solar Telescope), which means to observe axions that are produced in the sun by scattering X-rays off nuclei in a strong electric field [1]. There are a few other experiments under development like CASPeR [7], QUAX [4, 10], Dark Matter Radio [8], and ABRACABRA [20]. All have a different method and propose a different region of the axion mass range to probe.

Most experiments rely on measuring axions already present in the cosmic axion field, however, our experiment provides for another method where we can source the axions locally using them as force mediators for spin-dependent forces. We do not have to assume that they are a component of dark matter, leaving the mass range as the only real consideration needed. Figure 1.1 illustrates the basic

mechanism behind spin-dependent forces where the mass of one nucleon is coupled to the spin of another. Much like how gravity describes a mass coupling to another mass. ARIADNE proposes an experiment to carve out the green region in figure 1.2. This is accomplished since axions are the mediators for these spin-dependent forces. One thing to note is that this experiment would have significant implications beyond axion detection. It also provides a scheme to allow for an ultra-sensitive detection system which could provide the sensitivity for light massive boson searches [2, 27]. So the next thing to explore is spin-dependent forces.

QCD Axion parameter space

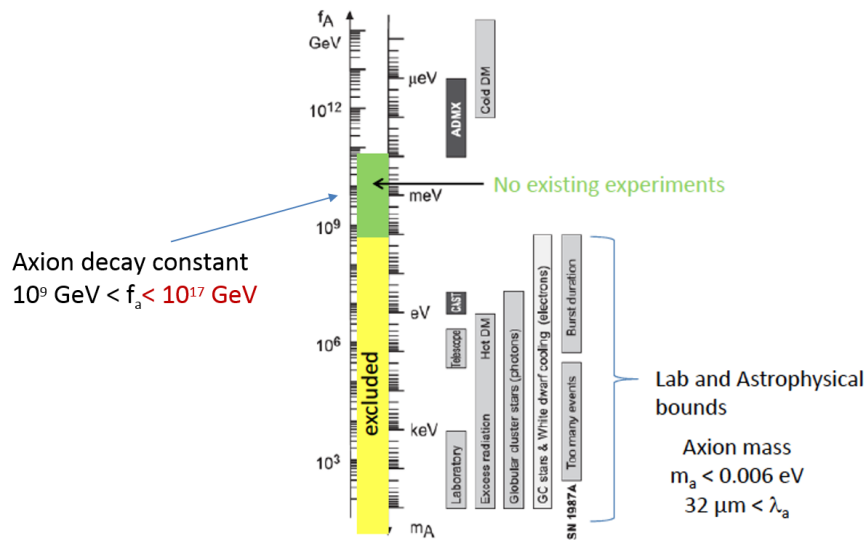


Figure 1.2: Current experimental bounds on the QCD axion mass range. Most experiments explore the ranges they are listed next to. ARIADNE aims to look at the green area where no current experiments exist [6].

1.2 Spin-Dependent Forces

The most significant piece of this puzzle and how to solve it lies within the spin-dependent force concept. All forces have an exchange that happens between two bodies that dictates the motion between them. For example, the electromagnetic force will mediate its interactions with photons; the strong force mediates forces between nucleons with pions and quarks with gluons. The weak force mediates forces with W and Z bosons. The concept is that interactions between all forms of matter have an associated force and thus a mediator that describes that interaction. The forces we wish to explore are the spin-dependent forces between nuclei.

$$U(r) = \frac{\hbar^2 g_s g_p}{8\pi m_f} \left(\frac{1}{r\lambda_a} + \frac{1}{r^2} \right) e^{-r/\lambda_a} (\hat{\sigma} \cdot \hat{r}) \equiv \mu_N \cdot B_{eff} \quad (1.1)$$

$$B_{eff} = \frac{1}{\gamma_f} \frac{\hbar g_s g_p}{4\pi m_f} \left(\frac{1}{r\lambda_a} + \frac{1}{r^2} \right) e^{-r/\lambda_a} \quad (1.2)$$

Equation 1.1 describes what we refer to as a spin-dependent interaction potential [2]. The important terms are as follows: g_s and g_p are coupling constants and depend on the axion's mass [2]; m_f defines the mass of the fermion; λ_a is the Compton wavelength [2, 22], which determines the range over which the axion interaction extends defined as $\lambda_a = \hbar c / m_a$. The range is determined by the mass of the axion (table 1.1) and can be as small as $30 \mu\text{m}$, which helps inform the decision of how far the mass should be located from the sample. B_{eff} is what we will define as an effective magnetic field, which will be discussed more later; lastly we also need to pay attention to the $\hat{\sigma}$ and \hat{r} , which represent the Pauli spin matrix and the vector separating the mass and spin respectively. The axion couples to $\hat{\sigma}$ which is proportional to the magnetic moment μ_N of the nucleus. What all this ends up

leading to is equation 1.2, which we have referred to as an effective magnetic field. This effective magnetic field is fictitious, for lack of a better term, and is produced by the coupling. Meaning that this field interacts with matter as a magnetic field would, but it also doesn't share all the same properties. For example, this field will not couple to orbital angular momentum, and also would not be affected by magnetic shielding techniques.

Seeing as we have this scheme for using the mass of one fermion coupled to the spin of another, we can begin to outline a technique for exploring this interaction. The most similar concept is that of Nuclear Magnetic Resonance (NMR). All nucleons have the intrinsic property referred to as spin. When said nucleon is placed in a magnetic field a known Larmor frequency can be determined (figure 1.3). A Larmor frequency is simply the precession of a nucleon's nuclear moment around the external magnetic field in which it is contained (equation 1.3). This precession is driven by a perpendicular time-varying magnetic field (equation 1.4). This time-varying field oscillates at the Larmor frequency and is then able to drive a resonant precession in the sample nucleon [2, 11]. This is the same concept used in MRI (magnetic resonance imaging) machines. The spin precession is driven by the nucleon absorbing and re-emitting the electromagnetic radiation. This re-emission is measured and in the case of an MRI is then used to create an image of the sample being measured.

$$\omega = \frac{2\mu_N \cdot B_{ext}}{\hbar} \quad (1.3)$$

$$B_{eff} = B_{\perp} \cos(\omega t) \quad (1.4)$$

The main difference between the traditional NMR scheme and the spin-dependent version is that we will use the axion generated field as our perpendicular field (equation 1.2). If the QCD axion mediates these spin-dependent forces, then we can use its interaction to generate an effective magnetic field. This fictitious field can be then used to probe the spins of the test sample. Lastly, this precession can be used to confirm the existence of the axion. While this is a vastly oversimplified explanation; a full explanation will be discussed in the following section.

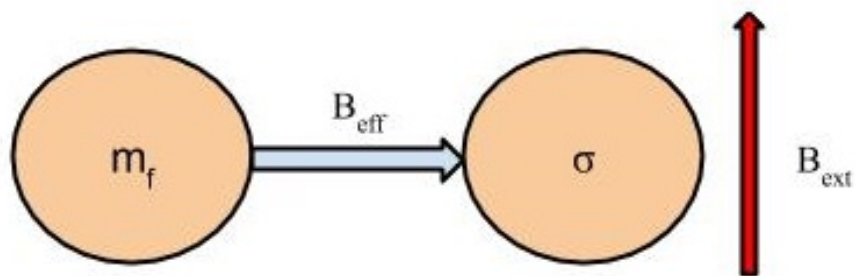


Figure 1.3: As with the depiction in Figure 1.1 the effective magnetic field produced by the oscillating mass interacts with the spin of the fermion in the external bias magnetic field.

1.3 ARIADNE Experiment

ARIADNE is a collaborative effort to search for the QCD axion using principles of NMR [2, 13]. If we take the NMR concept and apply it to an axion generated magnetic-like field, we should be able to use the said field to probe a known sample with a mass driven at some known Larmor frequency. The basic overview of the experiment as described in Figure 1.4 and features a few critical pieces. A spinning Tungsten sprocket is rotated to allow it to pass its teeth near a block which contains the sample spheroid full of Helium-3. A SQUID loop is used for magnetic field

detection. Not shown are a pair of D-shaped coils to supply a bias field, and a pair of correction coils to cancel gradients. While the concept is simple, in practice there is a myriad of factors and problems to solve. Each piece comes with its particular problems and considerations.

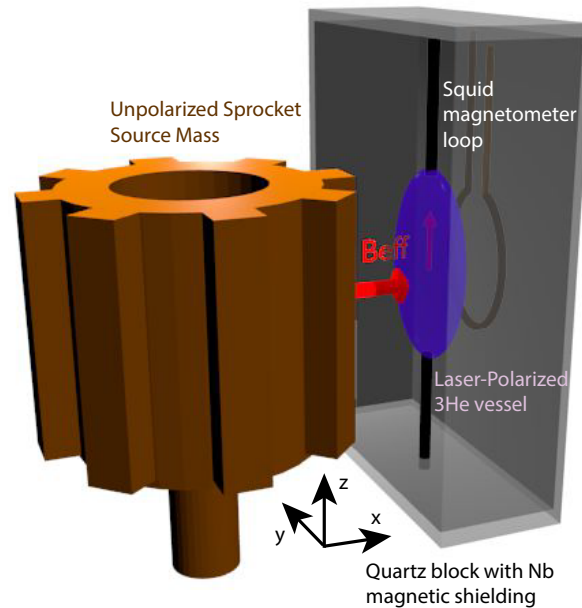


Figure 1.4: Setup: a sprocket-shaped source mass is rotated so its “teeth” pass near a laser-polarized ^3He NMR sample at its resonant frequency, producing a time-varying “fictitious” magnetic field via the axion potential. The resulting induced transverse magnetization is read out using a SQUID magnetometer. This distance between the rotating sprocket and He sample is kept within $\approx 200 \mu\text{m}$ to search for short-range axion-mediated forces [12]. Not to scale.

1.3.1 Spinning Mass

To effectively excite the Larmor precession of the Helium-3, we must modulate the amount of mass that comes within the range (λ_a) of the Helium-3 sample. One solution is to take a known material and machine it into a segmented cylinder,

or a sprocket-type shape, which allows for an oscillatory-type motion based on changing proximity to the mass, while also being able to control the frequency based on how fast the sprocket is spinning and how many teeth it has. There is another problem with this scheme, and that is ensuring that the speed at which the sprocket turns is very stable, which affords the ability to use the defined Larmor frequency defined by a known external bias magnetic field.

As seen in Figure 1.4, we can see the sprocket and the sample vessel. While the sample vessel has its issues, we want to focus on the sprocket for the moment. As we discussed having the speed and the dimensions figured out is very important, but the material is too. The rotating mass has a height of 1cm, an inner diameter of 3.4 cm, and an outer diameter of 3.8 cm which is divided into 22 sections of length 5.4 mm. Each tooth varies by $200 \mu\text{m}$, this is how the time varying field is produced. The mass has 11 teeth in total meaning that the frequency the sprocket rotates at is determined by $\omega = 11\omega_{rot}$ [13], which allows more flexibility for the motor rotational speed. Many motors that have been considered for this application cannot spin fast enough to generate the proper frequency, so adding teeth compensates for this feature but it also acts as a way to decouple the mechanical vibration from the signal. Another way to reduce vibrations or wobble is very much like balancing the wheels on a car. We can add mass to counterweight the source mass as a means to reduce vibrations and wobble.

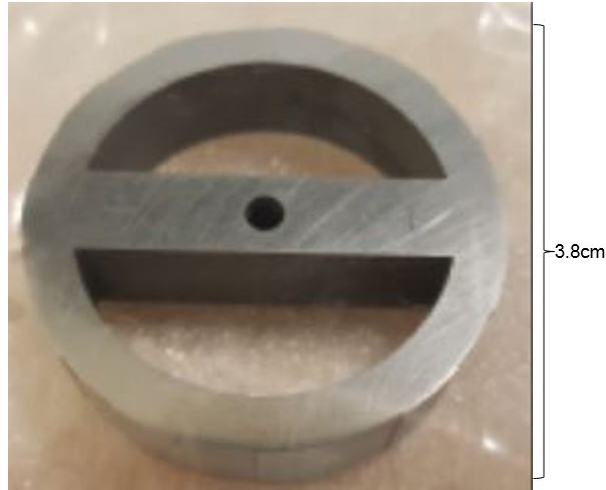


Figure 1.5: Example Tungsten source mass

1.3.2 Sample Block

The sample block has numerous parts and problems, most of which happen to be technical problems in production. For now, we want to discuss the baseline scheme behind the sample block. The first thing that we need to explain is why there is a need to contain most of the pieces inside a block. It is well established that the spin of a particle is affected by magnetic fields, and if we want to see the axion mediated effects, then it is in our best interest to screen as much of the background magnetic field as possible so that we can measure the forces intended. Seeing as we want to observe substantial effects on the spin, a gas that can be polarized and can maintain a high coherence time (T_2 time) is required. The coherence time refers to the time in which a sample is able to remain polarized, or before dephasing of the sample occurs [25].

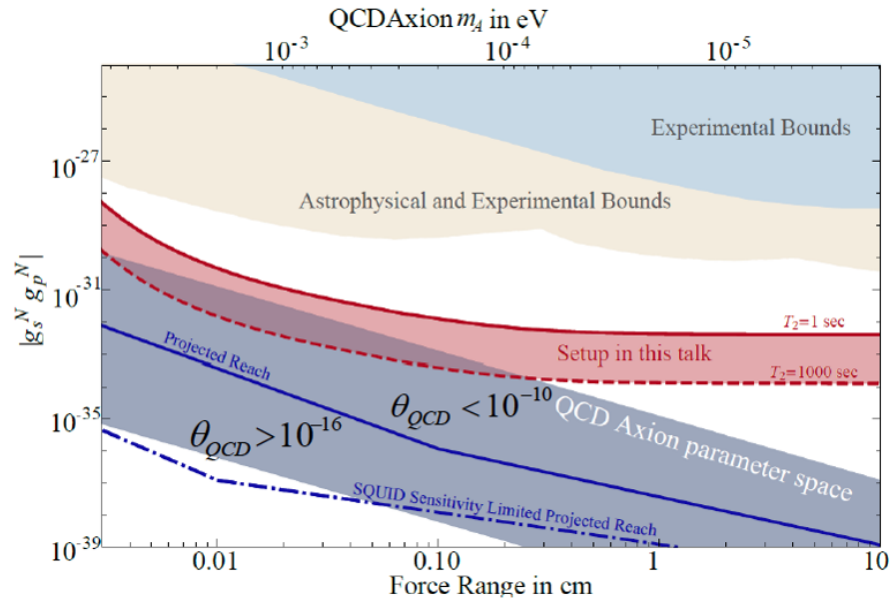


Figure 1.6: Axion parameter space as function of the axion force range and the coupling. The red band indicates the limits as defined by the transverse magnetization noise, a long T_2 time achieved by an integration time of 10^6 . The solid blue line indicates the projected reach based on potential future improvements. The bounds and current constraints are also shown [13].

Figure 1.6 shows the parameter space of all the current bounds on the QCD axion. First, the red band shows the limit of the experiment based on the integration time of 10^6 for a T_2 of 1 to 1000 seconds [25]. The limit this is set by equation 1.5 which describes the noise [2], leaving the noise significantly higher than the SQUID sensitivity. The dark blue band describes the reach of the experiment based on scaling up the experimental parameters. Based on those bounds we can determine some parameters for the experiment that we have to meet. The two important ones being the high T_2 time, and the SQUID sensitivity.

$$B_{min} \approx p^{-1} \sqrt{\frac{2\hbar b}{n_s \mu_{3He} \gamma V T_2}} = 3 \times 10^{-19} T \left(\frac{1}{p}\right) \times \sqrt{\left(\frac{b}{1Hz}\right) \left(\frac{1mm^3}{V}\right) \left(\frac{10^{21}cm^{-3}}{n_s}\right) \left(\frac{1000s}{T_2}\right)} \quad (1.5)$$

where B_{min} is the minimum transverse magnetic resonant field, p is the polarization fraction, V is the volume of the sample, γ is the gyromagnetic ratio for Helium-3 ($= (2\pi) \times 32.4MHz/T$), b is the bandwidth measurement, and $\mu_{3He} = -2.12 \times \mu_n$ is the nuclear magnetic moment for Helium-3 [7]. Using hyper-polarized Helium-3 gas it is possible to achieve transverse relaxation times on the order of what is required for the experiment [12, 25], that is if we can reduce external magnetic influences. The next issue, which focuses on the use of magnetic shielding to assist in screening the external influences. We chose Niobium because we can sputter it onto a surface and it is compatible with the temperatures needed for the Helium-3. However, what it does do is generate image spheroids. We know due to the method of images that the shield will induce magnetic gradients on the sample spheroid, thus there becomes a need for a method of controlling these induced gradients, and the choice to use a spheroidal geometry will be discussed in later chapters.

CHAPTER 2

DESIGN OF CHAMBER

Each piece of this project has a unique idea behind it, each with a unique challenge. In this section, each piece will be discussed in detail to outline the general thought process behind their solutions. Additionally, all challenges are discussed along with various ideas behind fixing them. For simplicities sake, we will break down the experiment into three main sections: the outer dewar and support structure, the middle plate, and the bottom plate. Each includes their own fascinating and unique components, which spawned the necessity for a diverse collaboration.

2.1 Bottom Plate

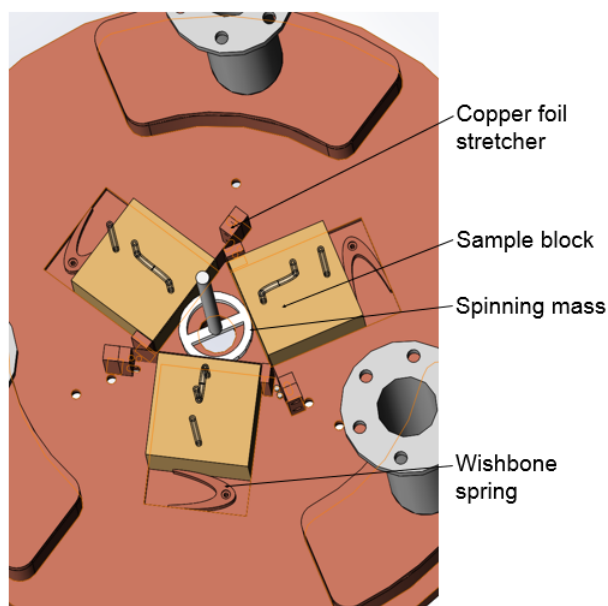


Figure 2.1: Bottom plate assembly.

Figure 2.1 shows the bottom plate, which is where many of the serious and

sensitive instruments lie, most notably the sample blocks. The bottom plate is made from copper because of its thermal conductivity and houses three liquid Helium reservoirs. These give the bottom plate access to a constant heat sink. This cools the superconducting shields on the blocks access to the proper temperature so they can maintain superconducting properties. The next part is the wishbone springs. These allow the blocks to be pressed against the front of their tracks. This is important because as the blocks become colder and everything begins to shrink, we want to maintain the samples position.

The motor is very hot relative to the rest of the experiment, and we want to prevent as much of the heat as possible from reaching the sample blocks. One solution that is planned on being implemented is the use of gold-coated copper foil. The foil is stretched between spring loaded copper posts. This again allows for some flexibility as the experiment changes sizes due to thermal fluctuations, and the copper foil gives an excellent thermal shield from any radiative effects from the spinning mass.

2.2 Middle Plate

The middle plate focuses around the drive system, as well as the various heat and magnetic shielding systems. The drive system (Figure 2.2) is the box mounted above the transparent middle plate, which is made of copper. (Note: much of the parts have been depicted as transparent for ease of viewing.) The transparent box in the center of the image is a small μ -Metal box that houses the motor. The box is also coated in gold to reduce black body heating [13]. The motor is attached to a drive shaft that starts in the box and extends down through the copper heat

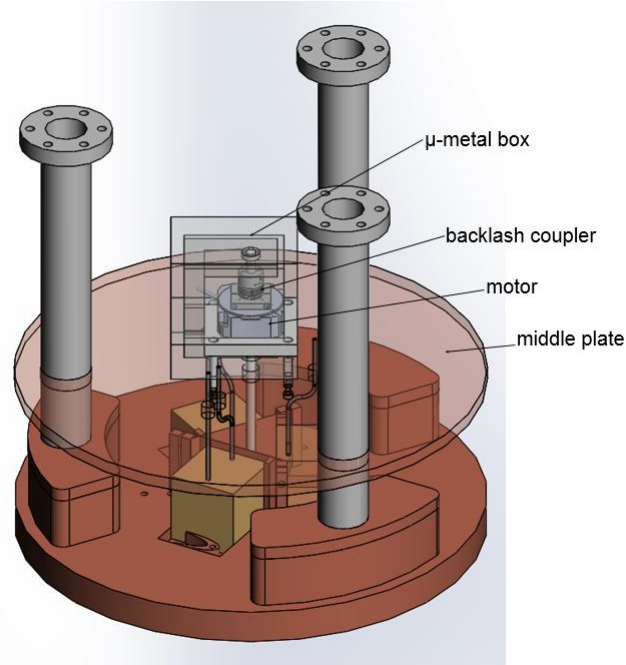


Figure 2.2: Middle plate configuration.

shield, all the way down to the spinning Tungsten mass located between the sample blocks. The reason we want to encase the motor is that the motor's operational temperature (-30°C) is significantly higher than the general environment of the rest of the chamber. Additionally, there are magnetic fields that are generated by the motor along with any associated connections that need to be made. So not only do we need to give the motor the proper environment to operate, but we also need to screen all the other components from the motor's operational needs. This is the reason for enclosing the motor in the μ -Metal enclosure.

We have devised a structure that we have named the C-Clamp. It is necessary for the piece that is intended to hold the bearings and provide a stable rotation point for the spinning mass. As discussed in Chapter 5, the C-Clamp is shaped like a 'C.' Embedded in the top and bottom plates of the C-Clamp is a ceramic bearing. The drive shaft runs up through the motor and is then coupled to the

motor by a zero backlash coupler. The purpose is to allow the bearings to provide the axis of rotation while allowing the motor to connect to the rod and supply the rotation.

There are two other portions of this region to be discussed, and the first is the tubes that are running from the bottom plate to the top of the Can which is not depicted in this figure. The Can isolates the outside environment which is mainly liquid Helium, from the rest of the experiment. However, these large tubes allow some of the liquid Helium-4 to flow down to the copper reservoirs so that the bottom plate can be held at a lower temperature more efficiently. Another piece that runs through this region is the tubes for the Helium-3 gas. The small glass tubes offer an inlet and outlet for the gas to flow in and out of the sample blocks. This gas is around 4.2K, so it does need to be slightly isolated from the liquid Helium. The glass tubes run from the top through the main column, down through the middle plate, and finally into the sample blocks.

2.3 Upper Section and Outer Dewar

The upper section is composed of the upper mounting structure, the heat baffles, and the outer cryostat dewar. This section is the most straightforward and is also the least fleshed out so far because the project is still young and there are other projects taking place first. The chamber thus far is thought to be hung by the top mounting structure, and then the outer dewar can be lifted into place over the primary experiment structure. The main column acts as a means to mount the main experiment chamber, but also to provide a passage for all of the instrumentation connections and for the plumbing to pump the Helium-3 to the chambers. Now the reason ev-

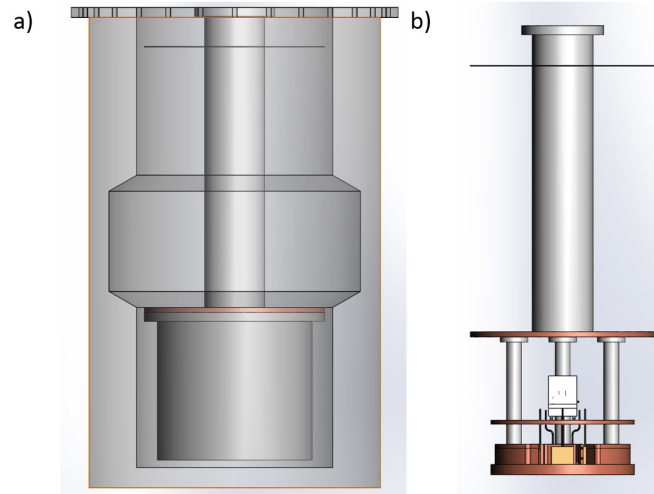


Figure 2.3: a) Total chamber with transparent dewar, b) total chamber with dewar and can removed.

everything needs to be separated in such a way is so that the different components can have their separate temperature zones. The outer dewar allows for pure liquid Helium-4 to bathe the Can and the lower plate, and the main mounting structure keeps temperature separate from the gaseous Helium-3 that is being pumped into the sample blocks. There is still much work to be done proving the other pieces of the project can achieve the sensitivity that is required for axion detection. So ensuring the details of the middle and lower plates are well thought out are of paramount importance. Such as the gas needs to be pumped from outside the entire system, through the tubing, and into the spheroids. Since the spheroid has a T_2 time between 1 and 1000 seconds, when the sample becomes incoherent, new Helium-3 must be exchanged for the old sample. Helium-3 is hyper-polarized by metastability exchange optical pumping (MEOP) [18] lead by our collaborators at the University of Indiana. They have been leading the charge on the hyper-polarized Helium-3 gas exchange system.

2.4 Design Final Remarks

The design discussed in the previous sections is mainly to give ourselves a rough roadmap for the work that needs to be completed. There are also various challenges that need to be solved that are not obvious from the model. For example, the motor is an area where we need to have a flexible operating temperature, but it should ideally have low magnetic noise, while also maintaining very stable rotation. Because to drive at the mass at the Larmor frequency, we have to know how fast the motor is spinning, and that it can very accurately maintain that speed. So determining which motor fits those criteria requires research and testing. Another example is the sample blocks having the ability to make connections with the tubes pumping fresh Helium-3 constantly, and feed-throughs for the SQUID and the correction coils. So all of those details do need to be considered. Additionally, how do we replace the Helium-3 in the spheroids, and make a connection with outside electronics without introducing magnetic field gradients into the sample blocks?

CHAPTER 3

MAGNETIC SHIELDING CALCULATIONS

In this Chapter, we will discuss the idea behind magnetic shielding and explore its viability. Furthermore, we discuss the problems that come with implementing the shield in a way that's actually useful and also some plans for block construction in the future.

3.1 Sample Geometry

It's important that the sample has a uniform magnetic field over its spatial extent, so as to maintain a constant Larmor frequency. It is also important that the bulk of the material is within a reasonable distance from the spinning mass. A straightforward geometry that can be uniformly magnetized is a sphere. The primary issue of the sphere is that the bulk of the material would not be held at a reasonable distance from the mass. However, use of an oblate spheroid will maintain these magnetic properties while holding the bulk of the material closer to the mass and has a constant interior field [26][12]. Refer to figure 3.1 for an example of the proposed layout of the sample location and shape, and spinning mass.

3.2 Method of Images and the Meissner Effect

The first step to detecting axions lies within the interaction between the sample and the mass. What we are looking to do is measure this fictitious magnetic interaction, but it is a short-range interaction that is also very small. In fact in order to

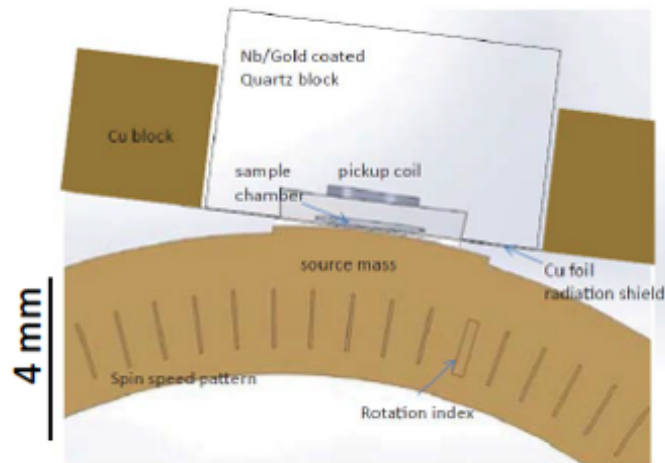


Figure 3.1: Example depiction of a top down cross sectional view of the sample vessel and the spinning mass.

be able to detect B_{eff} then we need to achieve sensitivity down to $3 \times 10^{-19}T$ at 100Hz [2]. This is difficult because all major sources of background magnetic field are on the order of $5 \times 10^{-5}T$ at DC [23]. Any magnetic field noise that might be generated by any equipment in the experiment itself or from impurities in the Tungsten mass are also factors. So there is a great deal of extraneous magnetic field noise that would distort measurements and make it difficult to detect axion related interactions. Now as stated before, this effective magnetic field is not screened by magnetic shielding. So, in theory, we should be able to isolate the sample from all external magnetic fields using a superconducting magnetic shield. Superconductors are advantageous over μ -metal because they can reduce magnetic field noise due to thermal currents such as Johnson noise. It also assists in reducing fields generated by thermal currents in the Tungsten mass which are measured to be on the order of $10^{-12}T/\sqrt{Hz}$ [13], and also screens the Barnett effect [5, 13] and any other noise generated by impurities in the sources mass. Initial testing of the mass done at PTB Berlin has shown minimal magnetic impurities at the surface of the pre-

liminary test mass produced by Stanford. Superconducting shields would be able to protect the magnetic properties and the Larmor frequency of the sample from outside influence and allows the ability to observe the effects from axion mediated forces. There is, however, a large consideration that deals with the images that would be generated by the shield. The Method of Images is a mathematical tool or representation of a boundary matching problem. It is mainly used to visualize how a charge interacts with a boundary or surface [21]. We can model this visually by there being an imaginary charge generated on the other side of the boundary. Its an image or a reflection in a mirror so to speak. So we can model the effects mathematically as two separate charges interacting with one another rather than seeing how the distribution of charges in the boundary has changed to cause this effect. It is a very powerful visual and mathematical tool to explore these effects.

First, before we talk further about images and controlling their effects, we first need to look at our sample and decide on some dimensions and locations. Firstly we chose the dimensions of the spheroid to be $3mm \times 3mm \times .15mm$ creating the pancake-like shape. As far as location is concerned, we wanted to place the edge of the spheroid at $75\mu m$ away from the wall of the container, which allows the sample to be kept within $\approx 200\mu m$ in order to adequately probe the appropriate range of the axion. Now that we have discussed size, shape, and location we can begin to discuss the image calculations. For starters we know what the field given off by a uniformly magnetized spheroid looks like[26] so we can see how the field is going to look like from the image.

We are asserting that the magnetic field in the spheroid sample is uniform. However, small perturbations in that field come from numerous sources, which is why screening out those effects is essential. The most significant perturbation

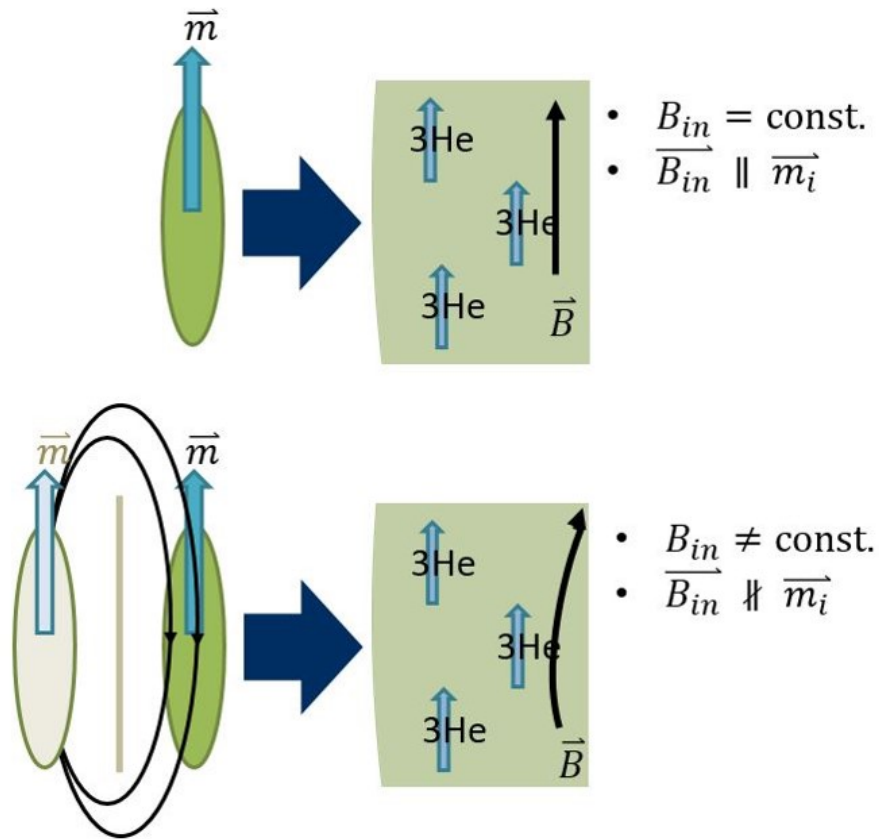


Figure 3.2: Meissner image generation example. Images show the relationship between the magnetic field B and the magnetization m .

stems from the sample's proximity to the superconducting wall. The Meissner Effect states that in the presence of a magnetic field, either generated by a magnetized object or current, then a superconductor will screen transverse magnetic fields by producing surface currents. In the case of a planar boundary, the image produced is identical to the real object, which is the most significant motivation behind making a planar boundary, but it has the added advantage of being easy to produce. Nevertheless, if we refer to figure 3.2 then we see that in the presence of the superconducting boundary, a Meissner image is produced, which induces a field on the real sample vessel. This is problematic because it no longer maintains the constant magnetic fields exist inside the sample. We need to drive all of the sample at the

same Larmor frequency (equation 1.3), but when there is a difference in magnetization from particle to particle that task becomes unmanageable.

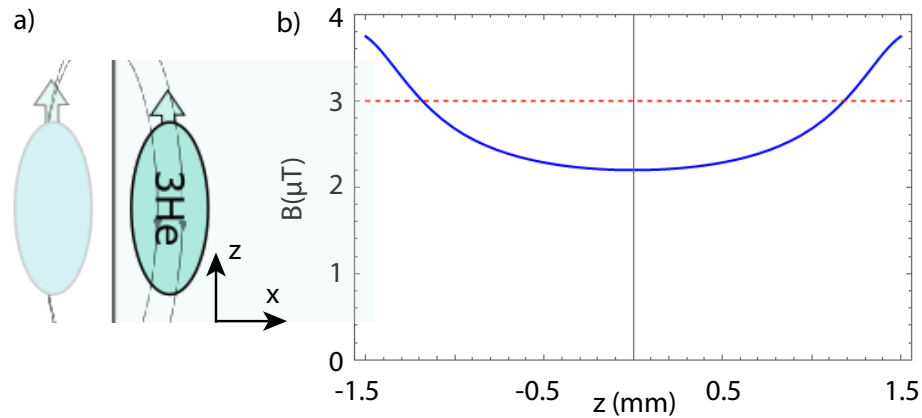


Figure 3.3: Example of what the magnetic fields look like inside the sample spheroid when in the presence of a Meissner image spheroid with a nuclear spin density of $2 \times 10^{21} \text{ spins/cc}$ and a DC bias of $\approx 3 \mu\text{T}$.

This perturbation produces a significant bimodal non-uniform magnetic field which does need to be canceled as well. Furthermore, there is the issue of higher order images that occur as an artifact of the sample block. Since the sample is inside a block, there are several images to consider from each wall. Thus we need to determine the higher order images, and the viability of canceling the effects from the "main" image, then we can attempt to reduce magnetic field gradients in the sample itself.

3.2.1 Higher Order Images

Now the goal is to explore the higher order images created by the other walls. To explain the issue imagine our sample vessel is between two walls equidistant on the left and the right. As discussed, an image will be produced to the left of

the left wall, and one to the right of the right wall. What we do know is that the transverse magnetic field at the surface is canceled by the image and the object. The field would not cancel at the location of the right wall due to the increased distance. The same is true for the image created by the right wall, which is what is referred to as a "second order" image. As one could imagine, this effect does not stop at second order, in fact, it would carry on indefinitely. However, there is a light at the end of this tunnel, that being each new set of images doubles their distance from the object thus decreasing their strength and effect. So the magnetic field between the plates would be roughly proportional to $\sum_{n=1}^{\infty} \frac{1}{(2nd)^3}$, which does converge. One way to model this is to essentially model it as an infinite lattice of cubes, each identical to the others; this allows us to see how each of them would affect the "real" spheroid's magnetic field gradients. It also gives us the flexibility to change the parameters of the boxes and see how to minimize these higher order effects quickly. It also allows for a clear path of optimization. One conclusion we reached is that we wanted to construct the box to have side lengths of 5cm, which gives us enough space to have all the other pieces but also helps reduce the higher order effects. Technically the larger the block, the smaller the higher order effects, but there is a point where that has diminishing returns regarding construction and field reduction. So we settled on 5cm side lengths for the block.

One primary consideration we had was how to effectively, not only in practicality but regarding cost as well, cancel or control the magnetic fields acting on the spheroid. The one aspect that has been alluded to but not elaborated on is the what was referred to as the "sample block." We know that our sample is a spheroidal shaped vessel to house the Helium-3 gas. Now the reason we went with the block shape was that it afforded us practicality regarding cost and production, it also gives us the planar surface to generate a perfect image spheroid. It also gives a flat

surface to place near the Tungsten mass. The most considerable advantage is that in an enclosed box we can screen out all external fields effectively, thus leaving us the task of needing to control only the fields inside the box.

3.3 Magnetic Field Correction

We have established that the fields inside the box do need some form of correction, so now we want to explore how to correct it and what types of parameters are needed. In the calculations, we have an infinite lattice of spheroid cubes using Helium-3 as the gas and a uniform magnetic field of $23 \mu T$ supplied by the external bias. Now for simplicity's sake, we set the fraction of polarization to 1, spins all aligned in the z -direction, and the nuclear spin density to 2×10^{21} spins/cc which correlates to the maximal spin density at 4.2 K [12]. A single spheroid produces a dipole field, so what we can do is find a way to generate a dipole field to cancel that of the image spheroid. The simplest way to accomplish that is to use a single loop of wire and run a current through it. Now, all that needs to be done is run a calculation that gives us four major parameters in which to optimize: box size, coil distance from spheroid, coil current, and coil radius. Scanning over these parameters provides a simple method of looking for the ideal configuration. The model is simple enough to where we can even add multiple coils in multiple locations, or even stack them to see if we can more accurately model the spheroid field. In this model, we employ the use of the statistical method of variance.

$$s^2 = \frac{\sum(x_i - \bar{x})^2}{n - 1} \quad (3.1)$$

Where s is the variance, x_i is the number in the group, \bar{x} is the mean, and n is the numbers in that group. In other words, this method allows us to scan over all the parameters and see how far off they are from the mean value for the magnetic field. So a small variance is what we are looking for, and will then tell us which parameters make that configuration ideal. However, there are two other optimizations that we can explore: one where we minimize the integral of the norm of the magnetic field across the sample (referred to as field cancellation), and one where we minimize the variance of the norm of the total field (referred to as gradient cancellation). Field cancellation has the advantage of telling us if the induced fields are canceled completely, which indicates the field over the extents of the sample is flat, i.e., the norm does not vary. However, the field is unidirectional and thus can be adjusted by a set of modified Helmholtz coils we call D-coils, which we will discuss in the next section. Nevertheless, we do have a means of "flattening the field." The Gradient cancellation method takes a different approach where it applies a field opposite the direction of magnetization, which allows for the field to fill in the gap, so to speak, to flatten the field. Through the optimization, we can figure out where to put the coils, how much current they need, which direction to run the current, and where spatially to put the coil. Referring to figure 3.4 we can how each method improves the "flatness" of the respective fields.

With the field cancellation method, we can reduce the variance of the magnetic fields by a factor of three using a coil diameter of 3mm, and current of 11.6mA. This method does allow for a high degree of tune-ability by just changing the current and seeing how the field develops. Now we are only getting a factor of 3 improvement because we are attempting to cancel a bimodal field with a unimodal field. So there is only so much that can be done concerning entirely canceling that effect out. With the Gradient cancellation method, we can reduce the variance by a factor

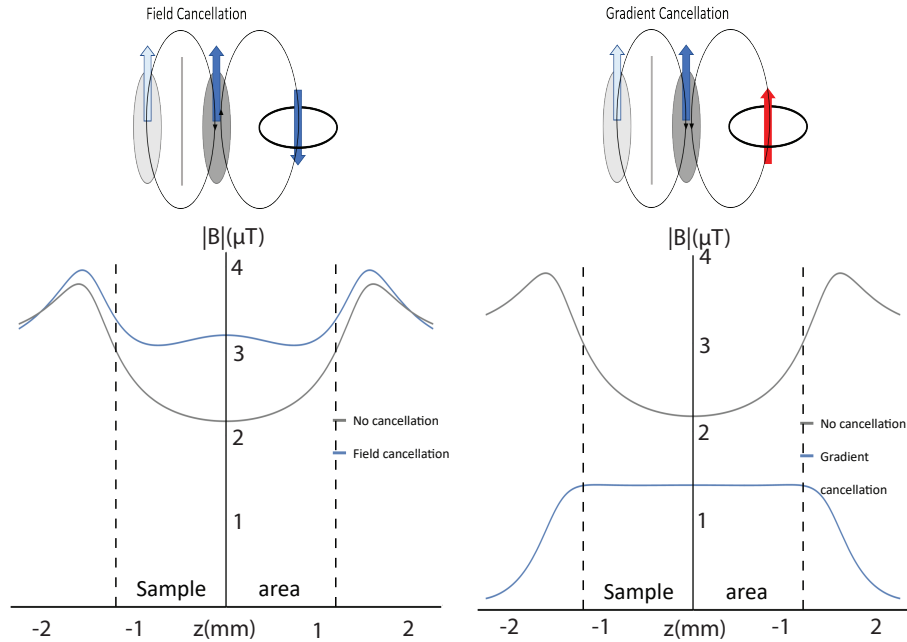


Figure 3.4: (left) The field cancellation method has the goal of canceling the field from the image spheroid by generating a opposing dipole field. (right) Gradient cancellation seeks to accomplish the same goal but by using a complimentary dipole field to minimize the variance from the norm.

of 10^2 over the inner 80 percent of the spheroid with a coil diameter of 3mm and a current of 1.6A. This works by providing a strong magnetic field anti-parallel to the magnetization. The gradient correction field falls off at about the same rate as the perturbed field so it "fills in the gap." Thus we can achieve a high degree of correction but a low degree of tune-ability because while the norm may be flat, the direction may not be consistent. The field and gradient cancellation methods can be run simultaneously or separately. In either case with this degree of cancellation the T_2 time can be achieved on the order of $\approx 100\text{s}$ [13], which puts us in the right area of our parameter space to search of axions.

3.3.1 D Shaped Helmholtz Bias Field

In most standard nuclear magnetic resonance experiments there is typically a large set of Helmholtz coils. These are used to polarize the sample and define a Larmor frequency, which is because Helmholtz coils maintain a uniform magnetic field over a large area through the central axis of the coils making them ideal for use in NMR because of the well defined magnetic field generated by them. Making them ideal for ARIADNE as well. There is one consideration, the proximity of the sample to the wall of the sample block. So not only will the field generated by the Helmholtz coils not be on axis with the sample, but it will also generate its own set of images across the boundary which could potentially complicate the magnetic field cancellation. One simple solution that would solve both issues is to cut the coils in half and turn them into what we refer to as D-coils. So they are Helmholtz coils but "D shaped."

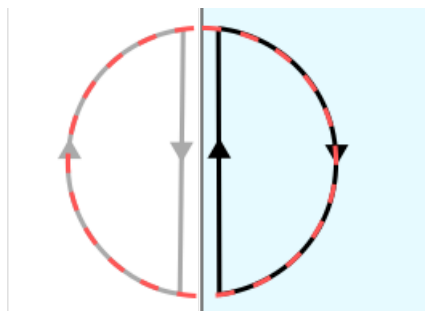


Figure 3.5: Example image of the D shaped Helmholtz coil with its associated image coil.

Figure 3.5 above shows the scheme of splitting a Helmholtz coil but still completing the coil with a straight segment completing the D-shape above. Now on the other side of the barrier is an image D-coil. Arranging it in this fashion affords us what we need to create that uniform field on axis. The fields generated by the straight segments will cancel resulting in the full magnetic field of a full

Helmholtz coil, which approximates the very field we are attempting to generate to polarize our sample. The approximation only get stronger the closer the coil gets to the boundary, and our only limitation is manufacturing limitations. However we obviously cannot entirely reduce the spacing, so the question becomes how that affects the overall field. In a typical Helmholtz configuration the second directional derivative of the magnetic field vanishes at the center, but with the D-coil configuration, this result is nonzero. So we need to determine what modifications need to be made to maintain that uniform Helmholtz field. One change that can be made is to increase the size of the coils because larger coils need more space between them to maintain the Helmholtz effect. However, there is an extra correction that helps to reduce this nonzero result coming from the D-coils. The D-coils need just a small amount of more space to account the added fields. For example, a 2cm field would need .4mm of extra space between each other, or a 3cm coil needs 4mm extra [12]. Luckily we have a large block to work with so increasing the size is possible within the block size we determined.

CHAPTER 4

BLOCK DESIGN

In this chapter, we want to discuss the challenges that face the sample block, as well as potential solutions to those problems. We also want to present some initial results from modeling and some proof of concept designs and physical models.

4.1 Magnetic Gradient Modeling

When we begin to take a look at the practicality of constructing a block like the one that will become the sensor system for ARIADNE we need to consider the various pieces that need to be embedded within, like the spheroid cavity, the correction coils, the SQUID loop, and the D-coils. All of these pieces perform an essential and necessary function when it comes to axion detection. Some are there to minimize internal magnetic fields, and others are for detection. The primary issues come in when we begin to discuss the practicality of making this scheme actually function. The major issues stem from how to make the necessary connections for all of the components, while also maintaining the ability to keep the gradients suppressed to a reasonable level. Figure 4.1 provides an example of the method of constructing the block. All pieces are present, but the major thing to note is that all the pieces have some connection to the environment outside of the box. These leaves clear paths for external sources of magnetic noise to penetrate into the box.

With the use of COMSOL Multiphysics [15], we can build a reliable model for how the magnetic field penetrates into the box. COMSOL is a powerful tool that allows one to build a particular geometry and then apply a whole host of physics

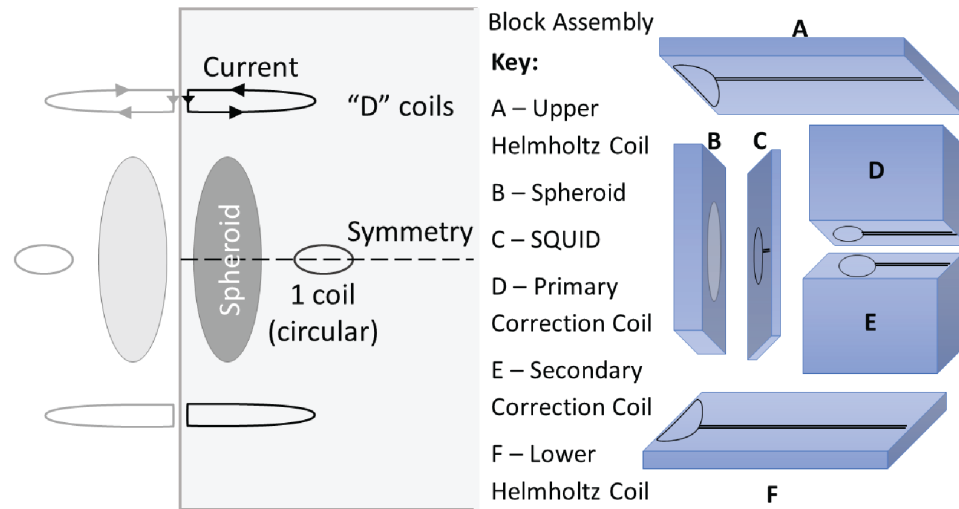


Figure 4.1: Schematic for the quartz sample block. This provides a scheme for how each component will be fabricated onto their individual portions of quartz, but also shows how they fit together. Once glued together, the block will be coated in Niobium.

to that configuration. The solver in the program uses the finite element method. In this case, we can program the block with the spheroid, designate the internal material as quartz, place a thin Niobium shell on the block, set a background magnetic field outside of the block, and observe how the fields react or penetrate into the box. If they do in fact penetrate the box, then is it at a level that is manageable? The initial tests of the shielding had the purpose of showing the shielding factor of a solid tube of Nb and a thin film of Nb coated onto glass. The tube dimensions were 200 mm in length, 23 mm inner diameter, 1 mm thick wall of solid Nb (figure 4.2 a)). The shielding factor achieved for this configuration is on the order of 10^9 . The associated COMSOL model showed a 10^7 shielding factor, which is comparable to the work done by J.R. Claycomb and J.H. Miller [9] who demonstrated a model of shielding factor for transverse magnetic fields in a superconducting tube (equation 4.1). Where z is the location on axis from the end of the tube, and a is the radius of the tube. Using 100 mm for z and 11.5 mm for a we get a shielding factor

of $\approx 10^7$.

$$\textit{ShieldingFactor} = \exp 1.84 \frac{z}{a} \quad (4.1)$$

The next tests are going to give a reference point for comparison against a thin film of Nb coated onto a glass tube, and also a glass tube that was cut in half down the axis and glued together before coating. The goal is to show the difference between solid Nb, thin films, and if glued junctions affect the shielding. The COMSOL model for a thin film coating was prepared to match the tests that our collaborators are looking to attempt. An initial thin film model for a 22mm inner diameter tube yielded a 10^7 shielding factor, but this will change based on the geometry that is decided on in the physical model. Much of the advising on the SQUID and shielding was provided by the collaborators from IBS and KRISS in South Korea, who has also been performing the physical testing. They are experts when it comes to SQUIDs and were paramount in assisting on design input, as well as testing of physical models.

The other issue we do have to keep in mind, however, is what to do if we take a component like the SQUID (Superconducting Quantum Interference Device) and follow its influence? The SQUID is a measurement device that needs access to its associated electronics via wires to operate. So one valuable idea to model is how to make openings for introduction of wires and how they affect the internal shielding factor. Unsurprisingly, just opening a hole in the shield allows a whole host of external noise to enter that stem from sources like the vibration of the mass, Patch effect, Johnson noise, Barnett effect, among others [13]. However what if we employ a superconducting tube, which is a hollow cylinder with open ends. In many textbooks, the outer material is considered to be "perfectly conducting"

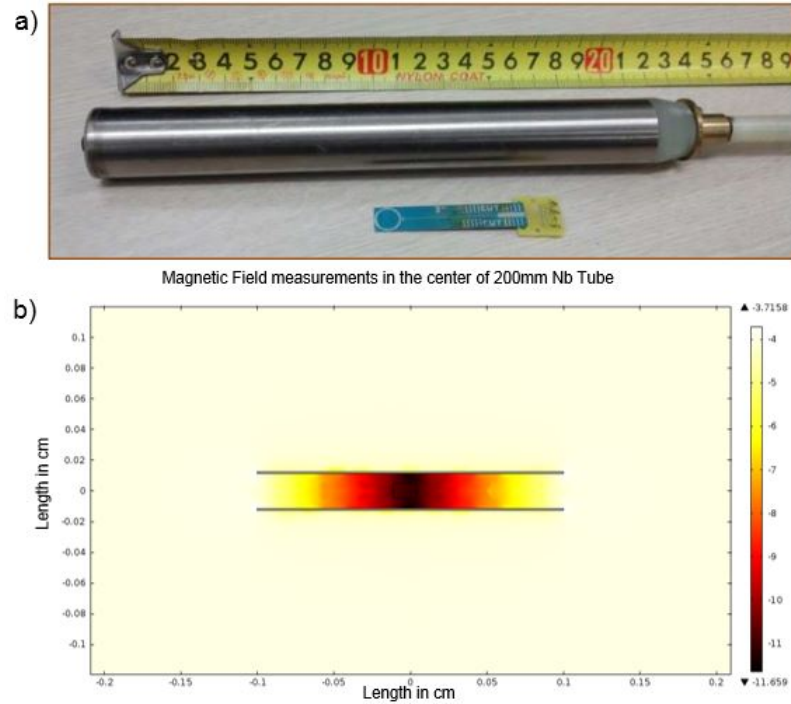


Figure 4.2: a) shows a solid tube of Nb used to measure the shielding factor. The tube was 200mm in length, 23mm ID, and the Nb thickness was 1mm. Below is the SQUID magnetometer used in measurement. b) Shows the COMSOL model of a the same solid Nb tube in an axial magnetic field to be used for comparison.

[19]. The goal of this tube is to cancel or terminate any electromagnetic wave that wants to propagate through the cylinder, which makes a this tube structure an ideal candidate for allowing connections to be made with outside influences while maintaining a high shielding factor. For example, if there is a magnetic field traveling parallel to a flat superconducting surface then there is no interaction between the field and the surface. Now if one takes that same surface and make a tube and allow the field to travel through the tube, then the surface currents generated will generate a field to oppose the on-axis field. Thus reducing the field and not allowing it to penetrate the tube. However, we do need to explore how much does it affect the field penetration and the shielding factor.

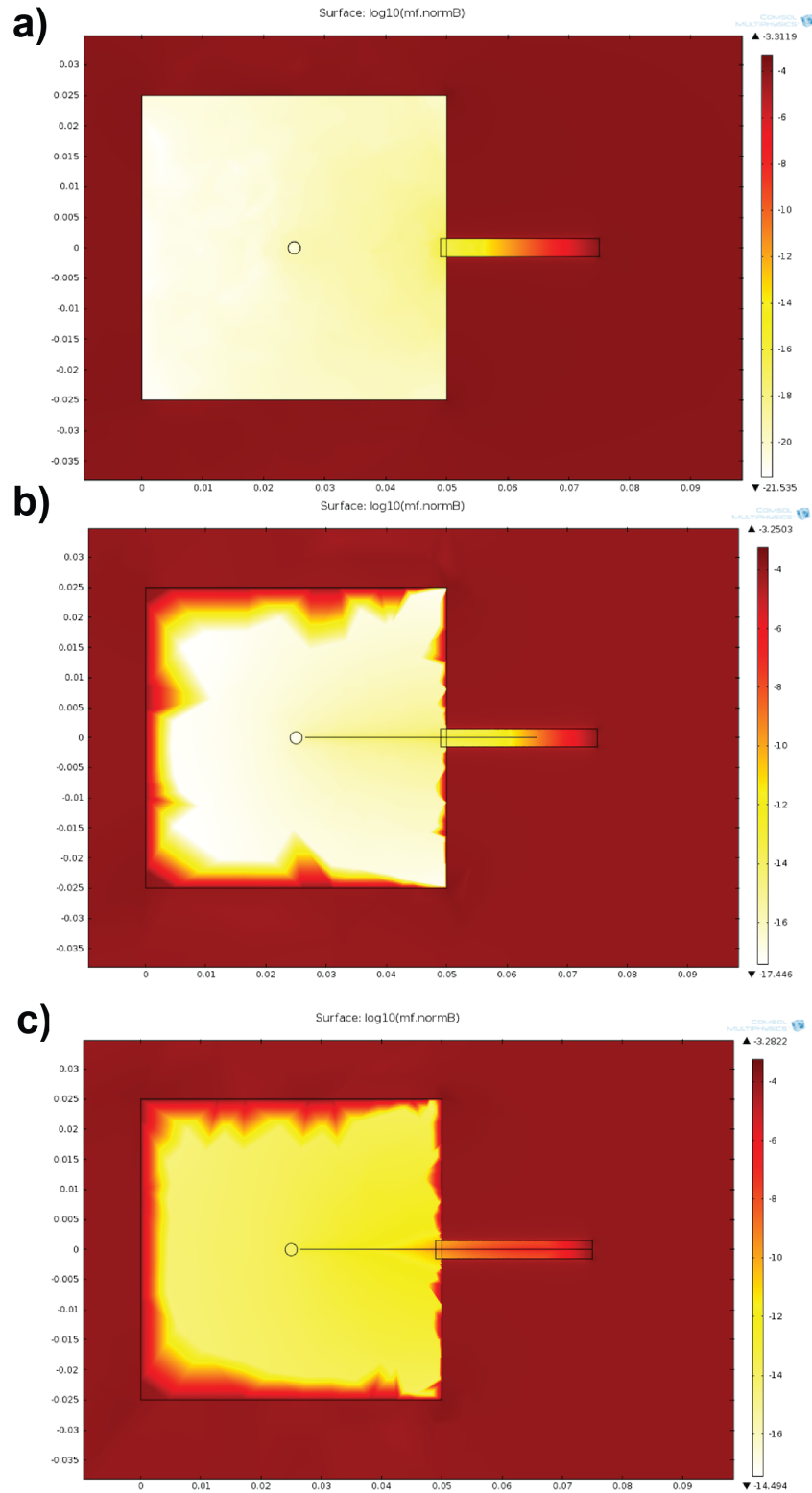


Figure 4.3: Plots of the magnetic field along the axis of the tube emerging from the superconducting shield, where the length of the superconducting portion of the central wire is varied from no superconducting wire, to one that extends to a point 10mm from the end of the tube, to one that extends to the end of the tube [12].

From Figure 4.3 plot a) we can see that the field penetration from a Niobium tube with a length of 15 mm and a diameter of 3 mm that the shielding factor for axial fields is on the order of 10^{15} and 10^{13} for transverse fields. This initial calculation shows that the idea behind waveguides is very applicable for reducing external fields attempting to enter the box. However, this is just a hollow tube with nothing inside. For both b) and c) we introduce a wire and observe how the field interacts with what is essentially an antenna. If we introduce a Niobium wire that starts 10mm from the end of the tube, then the effect from the wire becomes more evident. The field, while still low, penetrates much further into the block. It is also worth noting that the field that penetrates is slightly lower than where the wire starts. If we extend the wire to the end of the tube, then the field is seen to be significantly worse, on the order of 10^6 reduction in shielding factor which puts us below the desired shielding factor of 10^8 .

Generally, we should expect a minimal magnetic field penetration due to the nature of a waveguide. The problem comes from the fact that the wire is superconducting, and thus the field inside the tube forces the wire to produce currents within in itself. Lenz's Law causes the internal fields in the wire to reduce, but magnetic fields between the tube and the wire will increase. In a typical setup, the fields can terminate on the wire if it is a conductor, but since this is not the case, then the fields travel up the wire until they can terminate at the end. However, the end is embedded deep inside the box, so this means that the fields we are attempting to reduce, penetrate much further than intended. This result on its own is less than ideal, but there are a few things that we can do to mitigate this issue.

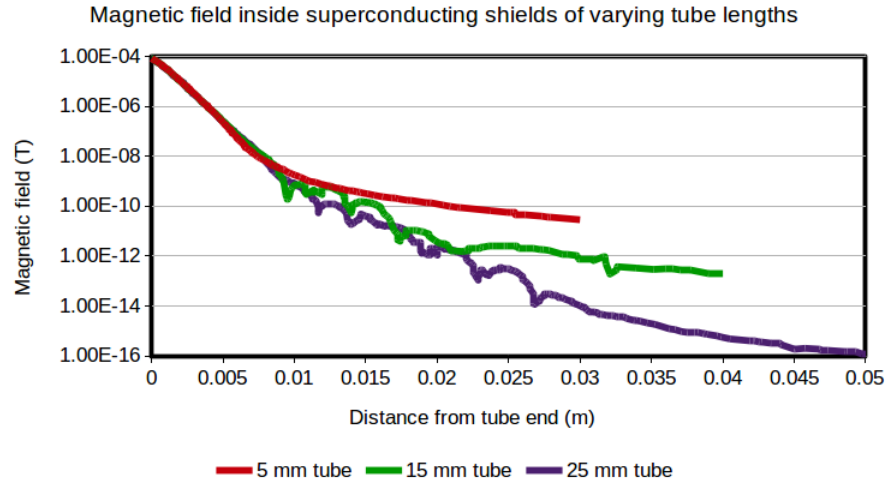


Figure 4.4: The line plots show the axial magnetic field penetration. Each line shows a different tube length, thus illustrating the effectiveness of different tube lengths without the presence of a central wire [12].

One adjustment that can be made is tube length. From Figure 4.4 we can see that increasing the tube length from 5 mm so 25 mm we can increase the shielding factor by 10^5 . However, that does not solve the issue of field penetration from the wires. As stated before, if the wire was of a normally conducting metal then fields will have a place to terminate. The main issues being that normal metals while also not exhibiting desirable superconducting properties, the Johnson noise produced would be high enough to drown out any small axion produced magnetic fields. One proposal is to take a small portion of the wire and replace it with Palladium. If we notice in Figure 4.3 that the improvement between plot a) and b) was not significant, therefore if we place the Palladium junction at the end of where plot b) is (15 mm from the block), then we should see a noticeable improvement as seen in Figure 4.5. With the junction, we reach a shielding factor of 10^{11} , roughly three orders of magnitude greater than what is required to achieve the necessary design sensitivity. Adding multiple junctions was explored, but was determined to not

add a significant benefit over the production challenges incurred.

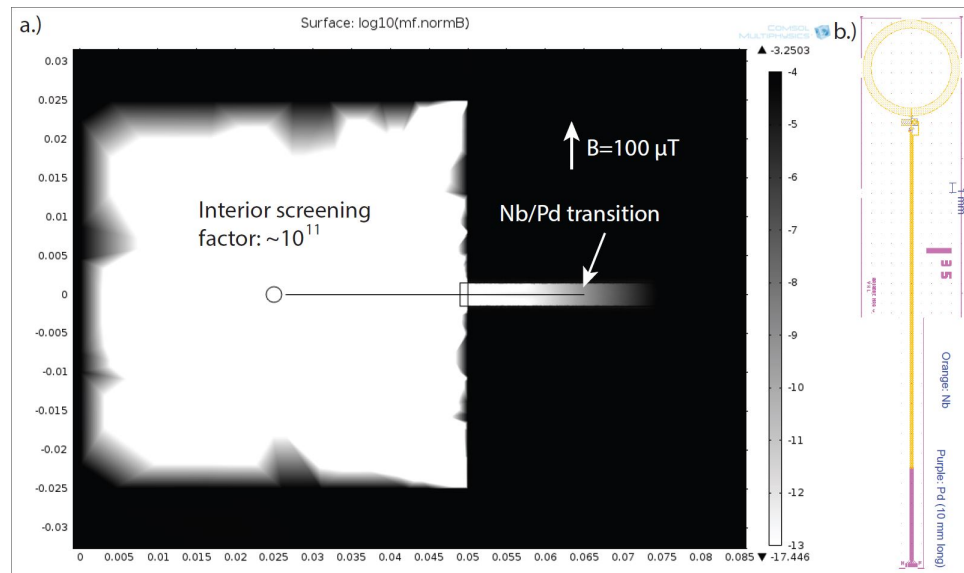


Figure 4.5: a) Plot showing the shielding factor when the Palladium junction is in place. b) Design of the SQUID loop to be implemented into ARIADNE.

4.2 Spheroid Machining and Block Design

One big challenge of the producing the block is machining the spheroid cavity. If we recall back to Figure 4.1 then we see the general layout of how to produce the block prior to coating with Nb. All of the wiring and coils can all be patterned onto the quartz pieces, but the spheroid and the inlet and outlet tubes must be machined into the glass. So the solution is to take two pieces of quartz and machine spheroid halves into them, then glue them together. In concept this is simple but due to the strange shape of the spheroid and the very small size of it, the problem becomes much more difficult.

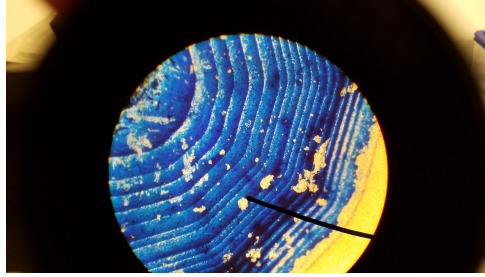


Figure 4.6: Machined spheroid half section example with $5\mu\text{m}$ steps. The Coloration is due to dyes that were used so a photo could be taken.

Figure 4.6 shows the first attempt at machining a spheroid. The most significant issue we had with this was that we did not know how the steps would effect gradients in the spheroid. We had modeled smooth spheroids, but not with steps. What we tried was to do an acid etching to smooth the steps (figure 4.7).

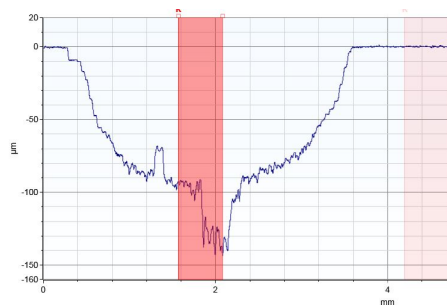


Figure 4.7: Profilometer data after applying failed acid etch to smooth steps.

The problem with the acid etch is that there is not a good way to keep the acid from pooling and making those deep features in the bottom as seen. The steps were reduced, but the bottom of the spheroid was ruined. The second set of spheroid halves produced by a milling process, and are awaiting profilometry measurements. There are other ideas on how to smooth these steps such as using an acid paste, or a mask to only allow the steps to come in contact with the acid.

Those are methods that could turn out viable. Additionally, we are in development to build a model of a stepped spheroid in COMSOL to see how it the steps effect the field in the spheroid.

CHAPTER 5

ROTATIONAL STABILITY TEST CHAMBER

The major goals of the ARIADNE project thus far have been to ensure that the sensitivity goals can be reached before heading into the development of the full experiment. All of the pieces need to be tested and verified for their efficacy. One area that needs to be verified is the mass drive-train region, previously referred to as the middle section. The goal of this proof of concept design is to develop a valid means of testing motor speed stability, mass wobble stability, and detection methods for verifying speed and wobble.

5.1 Chamber Design

Ensuring rotational stability is a major area of interest for ARIADNE to be able to detect axions. Because we are trying to detect short-range forces, the proximity of the mass to the shield is about $50 \mu\text{m}$. So the main problem becomes multi-tiered. Firstly, how do we maintain a mass wobble, meaning its sway from side to side, of less than $50 \mu\text{m}$. Second, how do we maintain the rotational speed stability of the motor? Third, how straight does the drive shaft need to be and what material should it be made of so it does not transmit too much heat to the sample chamber. Moreover, how do we measure the speed and the wobble? In the following sections, we will discuss the design, development, and initial testing of an apparatus deemed the Rotational Stability Test Chamber. Now we want to discuss the design of the test chamber and how it plans to help us characterize the motion of the spinning mass.

The rotational stability Chamber is designed to house a selection of two motors that were selected based on their range of speeds, operational temperature, and means of rotation as that dictates how much magnetic noise they give off. The two that were selected are the Aerotech brush-less direct drive servo motor and a Fukoku ultrasonic motor. The chamber was then designed to accommodate both for separate testing to determine the efficacy for use in ARIADNE.

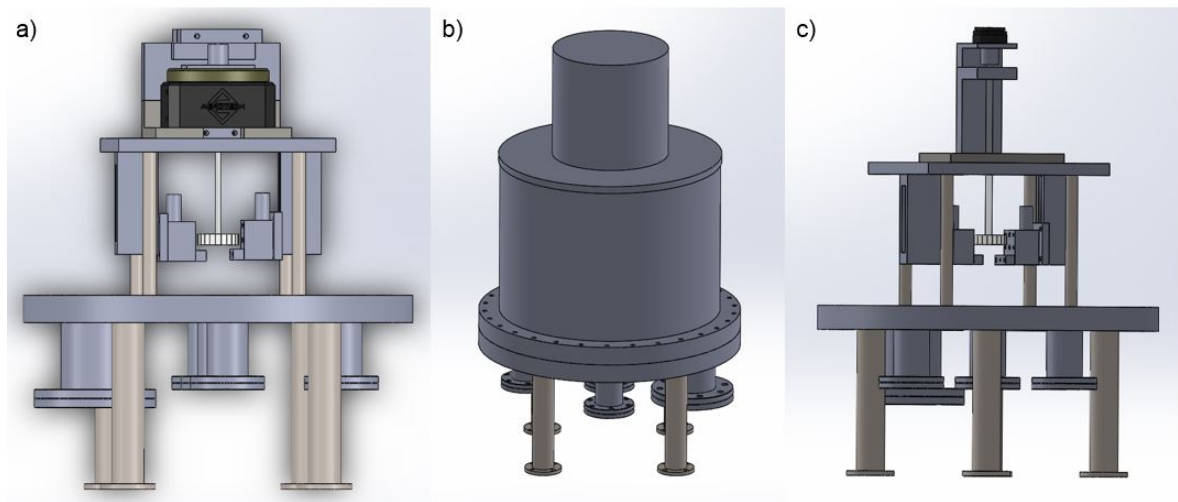


Figure 5.1: SolidWorks models of a) Aerotech chamber configuration with appropriate clamp design, b) chamber with top can attached, c) Fukoku motor configuration with appropriate clamp design.

Both motors have their own advantages and disadvantages starting with size. The Aerotech motor is significantly larger than the Fukoku motor, and thus structurally it demands more regarding total space required to accommodate it. On the other hand, the Fukoku requires special accommodations due to the height restrictions of the chamber, because of how it attaches to the rod. Thus the chamber extension shown in Figure 5.1 b). The Aerotech is a direct drive rotational stage while the Fukoku is a piezoelectric motor, so the magnetic noise given off is much lower from the Fukoku. However, the Aerotech can spin much faster (25 Hz) while having a great deal of control with the program that operates it. The Fukoku does

not have any control software, and due to its operation, it cannot achieve the same speeds (≈ 5 Hz). Most of these details will be discussed further in the following sections. The main features of the chamber are the clamps which house and secure the motor between two bearings and secure the rod to the motor, the rod and mass assembly, and the support structures that hold two fiber interferometers which will be discussed later.

5.1.1 Aerotech Motor Configuration

As depicted in Figure 5.1 a) the configuration is rather simple. Embedded in the top and bottom plates of the clamp there are two ceramic bearings. The ceramic bearings are useful because of their lower thermal expansion rates and their ability to be used dry, meaning there is no lubrication, which is because they will eventually be used in cryogenic conditions. Mounted to the lower plate is the motor and on top of the motor's stage, there is an adapter which allows the backlash coupler to take hold of the motor. The backlash coupler then holds onto the rod which extends from the top plate through the motor and down to the mass. The main reason for the bearings is to give the mass an axis to rotate around; the motor is just there to impart the rotational motion and not to provide the axis, thus the backlash coupler. There are two support structures that provide a significant degree of vertical motion. There are 1D vacuum stages mounted to the structures so a fine adjustment can be made to the fiber interferometer's distance to the mass. The interferometer is the tool we use to measure the distance from the tip of the fiber to the mass. The whole system is designed to be tested under vacuum. The initial tests will not be performed under cryogenic conditions. However, we can perform many of preliminary tests under vacuum to help get an idea of what happens to

the system under vacuum.

5.1.2 Shinsei Motor Configuration

With the small motor (Figure 5.1 c) the significant difference comes from the size of the motor and how the rod will attach to the motor. Unlike the larger motor, the small motor does not have a hole in the middle to pass the rod through. It has a post that comes off the top and will attach to the rod via the backlash coupler. The clamp configuration is in more of an 'E' type shape rather than a 'C,' which is because there is still a need to use both bearings, but the top bearing is in the center plate below the coupler and the lower bearing in the bottom plate. Additionally, so both motors can be tested under the same conditions, the bearings have the same spacing on both clamp configurations. The overall configuration for the small motor is taller thus the need to cut a hole in the top and add a chamber extension that is welded to the top of the can to accommodate the extra height.

5.2 Motor Rotational Speed Stability

One critical aspect of the rotational stability is to provide a constant Larmor frequency for the mass to oscillate. To ensure the proper Larmor frequency is not only provided but also maintained then we must be able to monitor the speed of the motor. Fortunately, the large motor, because it is an advanced rotational stage, has a very sophisticated program to operate the motor. So for the initial test of the speed stability, the large motor can be monitored via its built-in optical encoder. This test is done under no load in air. The data in Figure 5.2 shows motor stability

at one part in 10^4 of a given speed, with an rms variation at \sim one part in 3000. With speed stability of this magnitude, the sample can remain on resonance and utilize a $T_2 > 100\text{s}$ [13].

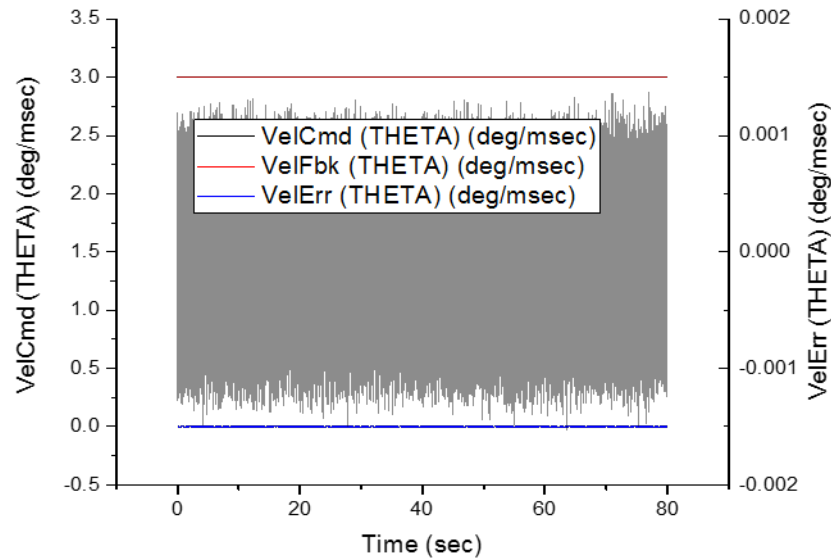


Figure 5.2: Spin speed stability provided by the Aerotech built-in optical encoder performed under no load and in air. VelErr is the velocity error signal, VelFbk is the feedback signal, and VelCmd is the velocity command signal.

The small motor does not have the advantage of the advanced control software. It is a more straightforward motor with an external driver. The best way to run an initial test of this motor is to run what we called the "Police Siren Test." What this test consisted of is a standard Helium-Neon laser, a photo-detector, and an oscilloscope. The shaft that protrudes off the top of the motor has a flat area usually reserved for a set screw to fasten something to the shaft. Instead what we did is use its flat reflective surface to bounce the laser off and into the photo-detector. Thus simulating the lights on a police car. So as the shaft rotates, we can see how fast it passed the detector and understand how fast the motor is spinning.

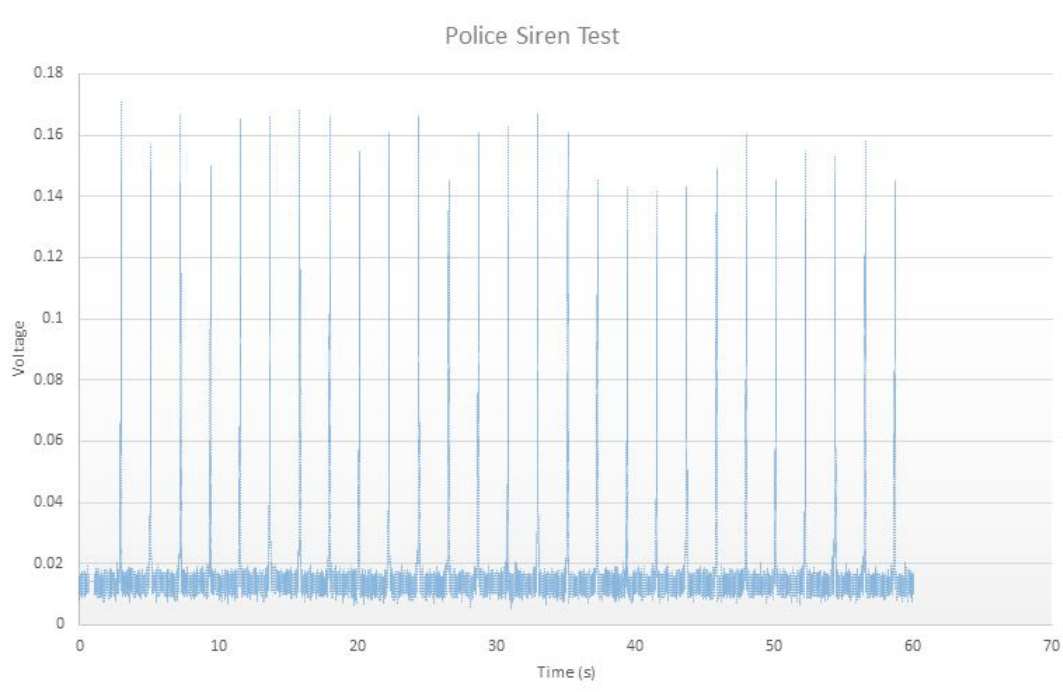


Figure 5.3: Spin speed stability provided by a basic photo detector. The spikes in the data represent each time the HeNe laser passes the detector. All of the base line noise is due to ambient light in the room at the time of measurement.

The data helped us understand and confirm the spin speed of the motor, however as time goes on the motor speed drifts over long periods of time. Thus we need a way to maintain and monitor the speed of the motor. One way we will monitor the speed is an etched pattern on the spinning mass. The interferometer will monitor distance and speed based on these notches. The major change between the motors is that the program required to monitor the speed of the mass will then be adapted to be a feedback system for the small motor. When the program sees a dip or spike in the speed it can adjust the motor speed by adjusting the supply voltage for the motor. With the large motor, this is not required, but the speed monitoring as the second point of reference is desired. This program is currently under development so much of the following discussion will be using the large motor.

5.3 Test Mass Assembly

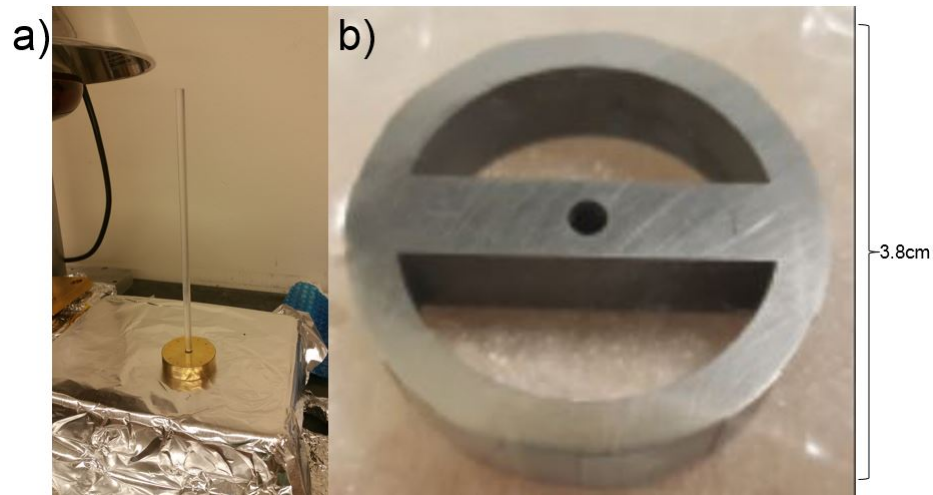


Figure 5.4: a) Brass test mass with timing grooves and glass rod inserted via hot plate and allowed to cool. The brass contracts to the point of holding on to the rod. b) Example Tungsten mass.

The test mass itself is very simple; it is simply a piece of brass machined to be the same size and weight of the Tungsten source mass. The Tungsten mass is not completely solid, see Figure 5.4, so this accounts for the difference in mass between Tungsten and Brass. The rod is a bit more complicated due to the amount of precision required. The dimensions for the rod were requested as: diameter is $5 \pm .01\text{mm}$, the length is $7.5 \pm .1''$, the ovality is $< .0004''$, and the total run-out (or bow from end to end) is $< .001''$. The first plan was to use glass as the rod material; the major issue becomes the process of how to produce rods. Most glass rods are produced by a centerless grinder; this is because it is challenging to machine glass especially when the diameter is so small, as is true for our rods. The centerless grind is very good at obtaining the ovality and diameter measurements, but not as good at obtaining the total run-out (TOR). The main method of producing rods is to run one long rod through the grinder and then cut them to size afterward. After

attempting two different runs of glass rods with different companies and different methods, only 10 percent of the rods were usable in the experiment (Table 5.1).

Table 5.1: Glass Rod Dimension Data in inches

Rod Number	Diameter 1	Diameter 2	TRO
1	0.1972-0.1972	0.1970-0.1969	0.004
2	0.1970-0.1971	0.1972-0.1972	0.003
3	0.1971-0.1972	0.1972-0.1972	0.0042
4	0.1968-0.1967	0.1970-0.1970	0.0047
5	0.1971-0.1971	0.1972-0.1972	0.0032
6	0.1971-0.1971	0.1970-0.1970	0.0032
7	0.1971-0.1970	0.1971-0.1971	0.0035
8	0.1973-0.1973	0.1970-0.1969	0.0025
9	0.1970-0.1970	0.1967-0.1967	0.0045
10	0.1968-0.1966	0.1969-0.1968	0.0042
11	0.1972-0.1973	0.1971-0.1972	0.003
12	0.1971-0.1972	0.1965-0.1974	0.0015
13	0.1973-0.1971	0.1976-0.1975	0.0025
14	0.1977-0.1976	0.1971-0.1972	0.006
15	0.1971-0.1972	0.1972-0.1972	0.0065
16	0.1972-0.1972	0.1977-0.1976	0.002
17	0.1974-0.1973	0.1972-0.1972	0.0025
18	0.1971-0.1972	0.1979-0.1978	0.0045
19	0.1973-0.1974	0.1974-0.1972	0.007
20	0.1972-0.1972	0.1975-0.1972	0.009

This is not ideal because rod production is resource intensive, however for the first set of tests we did move forward with the glass rods. The test fits for the mass onto the glass rod was an interference fit of 0.002 mm. The brass mass was placed on a hot plate to allow it to expand; then the rod was placed in the hole. As the mass cooled it should take hold of the rod and stay in place. The interference fit is ideal due to maintaining concentricity between the rod and the mass. The problem was that the glass was unable to handle the pressure applied by the shrinking brass. So in the spirit of moving forward with initial testing, we opened up the hole on the brass and glued a rod into place. We then explored some other materials to replace the glass. We looked into a Titanium alloy (Ti6Al4V) and Alumina. Both

have poor thermal conductivity, both have low magnetic properties, and can be machined. However the Ti alloy is much cheaper than the Alumina, so we started with a run of Ti rods and are optimistic about their efficacy, but there are further tests that need to be performed. See table 5.2 for Titanium rod dimensions.

Table 5.2: Titanium Rod Dimension Data in inches

Rod Number	Diameter 1	Diameter 2	TRO
1	0.1972-0.1972	0.1970-0.1969	0.0003
2	0.1970-0.1971	0.1972-0.1972	0.0006
3	0.1971-0.1972	0.1972-0.1972	0.0005
4	0.1968-0.1967	0.1970-0.1970	0.0008
5	0.1971-0.1971	0.1972-0.1972	0.0005
6	0.1971-0.1971	0.1970-0.1970	0.0007
7	0.1971-0.1970	0.1971-0.1971	0.0005
8	0.1973-0.1973	0.1970-0.1969	0.0004
9	0.1970-0.1970	0.1967-0.1967	0.002
10	0.1968-0.1966	0.1969-0.1968	0.0006
11	0.1972-0.1973	0.1971-0.1972	0.0003
12	0.1971-0.1972	0.1965-0.1974	0.0002
13	0.1973-0.1971	0.1976-0.1975	0.0005
14	0.1977-0.1976	0.1971-0.1972	0.0007
15	0.1971-0.1972	0.1972-0.1972	0.001
16	0.1972-0.1972	0.1977-0.1976	0.0008
17	0.1974-0.1973	0.1972-0.1972	0.0009
18	0.1971-0.1972	0.1979-0.1978	0.0005

Another test we performed was a test fit of the bearings onto a Titanium rod. The bearings, much like the mass, require an interference fit. So what we can do is cause one to expand or contract to conform to the other. The problem is that the ceramic bearings were chosen based on their ability to operate without lubricant, but also their extremely low thermal expansion properties. So the way to fix the bearings to the rod was to cause the rod to contract with liquid Nitrogen. The Titanium reacts to the temperature in a much more drastic way so we can use this method to slowly press the bearings into place 5.5.

Upon which time we can remeasure the TRO to verify if the rod maintained

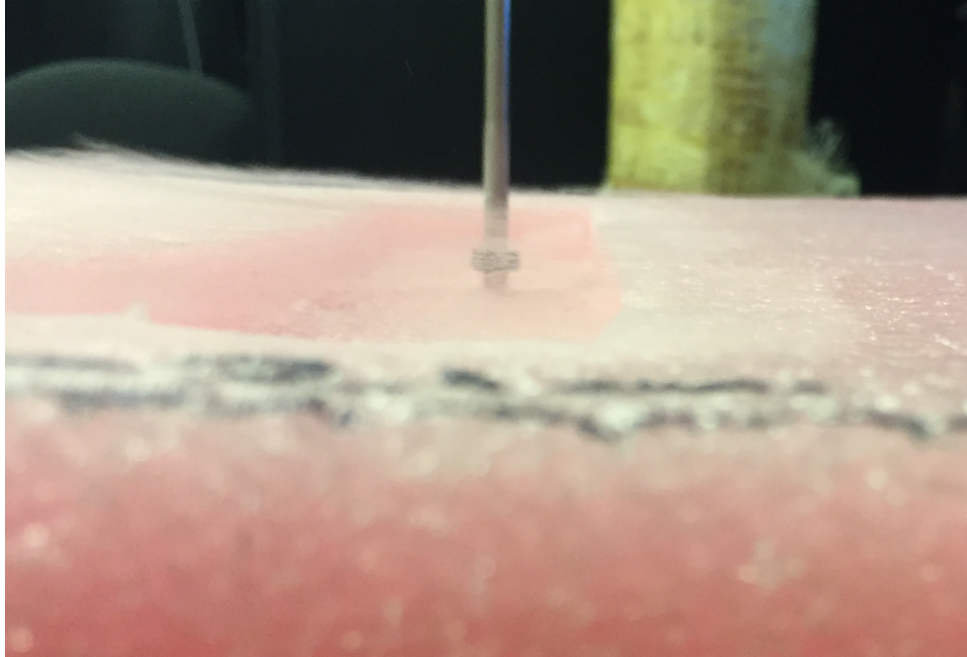


Figure 5.5: Shows a Titanium rod with the center bearing being pressed into place via liquid Nitrogen. The rod is dipped in liquid Nitrogen at one end to allow the Titanium to cool while isolating the bearing as much as possible.

its ideal dimensions. For example, we refer to the rod used in figure 5.6 which happened to be rod number 3 from table 5.2. The TRO began as .0005", and after affixing the bearings, it reduced to .0003". It was a drastic reduction. However, it still is well within the desired range of TRO. The last modification that needs to be made at this point is to the C clamp based on the findings with fitting the bearings to the rod. Figure 5.7 a) shows the modified clamp. Since the bearings have to be pressed into place with liquid Nitrogen, it means that we have to assemble the and affix the motor and coupler onto the rod before the bearings are in place, which makes it difficult to then insert into the clamp. However, with the new bearing cap configuration, it allows for easy access to slide the motor-rod assembly into place, then place the caps in to hold the bearings.



Figure 5.6: a) Shows a Titanium rod with both bearings fixed into place via liquid Nitrogen. b) Shows the jig made to test the TRO of each rod both with and without bearings. The jig holds the rod in the places where the bearings would be. As the rod rotates the dial reads the total deflection of the end of the rod.

5.4 Interferometer

The fiber interferometer is the tool we chose to aid in assessing the wobble of the mass. A fiber interferometer uses fiber optics instead of just straight runs of open space. One improvement is their ability to make high precision measurements while also taking up very little space. Using a 1310nm fiber coupled laser, we can split the laser signal between a reference fiber and a fiber that runs to the experiment. The experiment fiber measures interference between light that bounces off the target and the end of the fiber.

Initial testing of the interferometer was done using a piezoelectric mirror. Varying the distance of the mirror with a ramp box we can generate an interference pattern and discover the fringe visibility. Using equation 5.1 we can calculate the total visibility of Figure 5.9 as 0.13, which give us a sensitivity of about 160 nm/V.

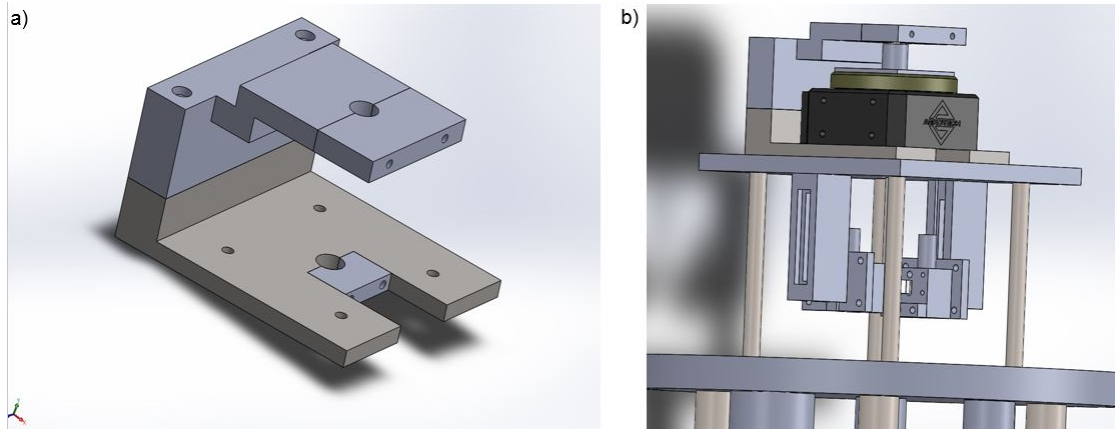


Figure 5.7: a) Shows the modified clamp with the new bearing caps. The purpose is to allow an easy way to insert the motor assembly and hold on the the bearings. b) Shows a zoomed in model of the complete large motor assembly.

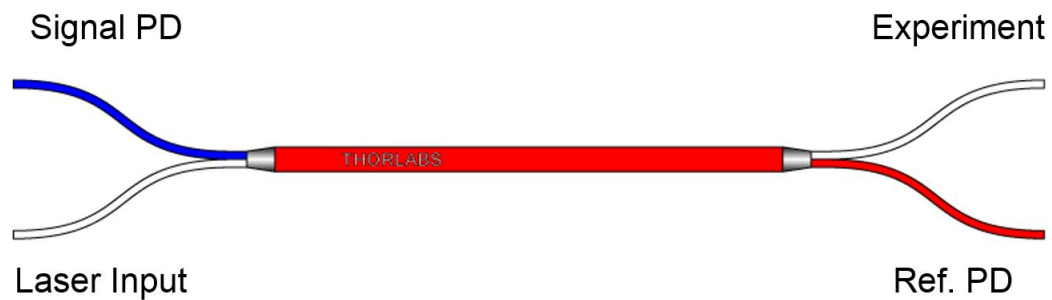


Figure 5.8: Example of the scheme behind the interferometer using the fiber splitter. The signal PD is how we collect the interference from the experiment and compare to the reference.

Giving us more than enough sensitivity to accurately measure the wobble of the mass.

$$v = \frac{I_{max} - I_{min}}{I_{max} + I_{min}} \quad (5.1)$$

Normally it would be advantageous to measure the wobble from the side of the mass. However, as figure 2.1 shows, there isn't space to input a fiber from the side.

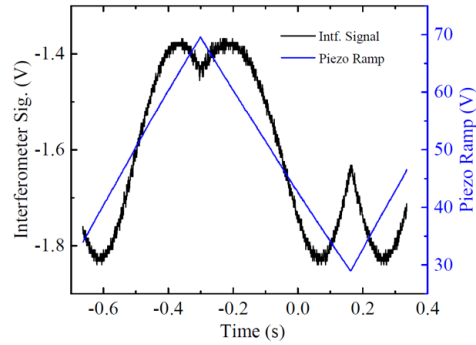


Figure 5.9: Signal generated by the interferometer interacting with a piezoelectric mirror.

So measuring the top or bottom of the mass is required. It also gives the flexibility to implement timing notches to monitor speed. We want to measure distance 'd' using the interferometer. We can measure the vertical change in distance based on the number of fringes we transitioned through. However, we want to know the horizontal change in distance. Through using equations 5.2, 5.3, 5.4 we can arrive at the desired horizontal deflection or wobble.

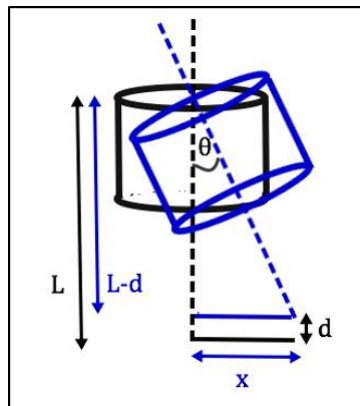


Figure 5.10: Geometric example of the wobble of the spinning mass. It indicated the important variables in order to determine the wobble distance 'd' and thus the horizontal wobble 'x'.

$$\theta = \cos^{-1}\left(\frac{L-d}{L}\right) \quad (5.2)$$

$$d = n \frac{\lambda}{2} \quad (5.3)$$

$$x = (L - d) \tan \theta \quad (5.4)$$

5.5 Results

There are a few pieces still under construction, such as the C and E clamps, as well as the program for controlling the speed of the small motor. Thus the goal of the initial testing of the apparatus is to verify the systems are working as intended. The initial testing of the chamber is possible using the glued mass-rod combination and a temporary adapter for the large motor, which fastens the rod to the motor with a single nylon screw. The other major difference for the initial test is that the apparatus will not be under vacuum, and will be open to the environment. Additionally, only one of the interferometers was used due to technical issues with the other. Nevertheless, only one is needed for the initial test because the goal is merely to see if the measurements from the interferometer make sense physically. For the rod, we used rod number 6 as the test rod (Table 5.1), which was chosen because at the time we were not aware that we were moving to Titanium rods from glass. So since this rod was going to be destroyed eventually, we chose one that would have never been used in the experiment regardless, due to its TOR being so poor. One other change that we made was to glue a $\lambda/10$ silver mirror to the bottom of the mass, because the interferometer is sensitive enough to measure small imperfections in the surface of the brass. The test mass was not polished, which left a large amount of noise when using the interferometer. The solution was

intended as a quick fix to ensure that we verify the interferometer is reading valid measurements.

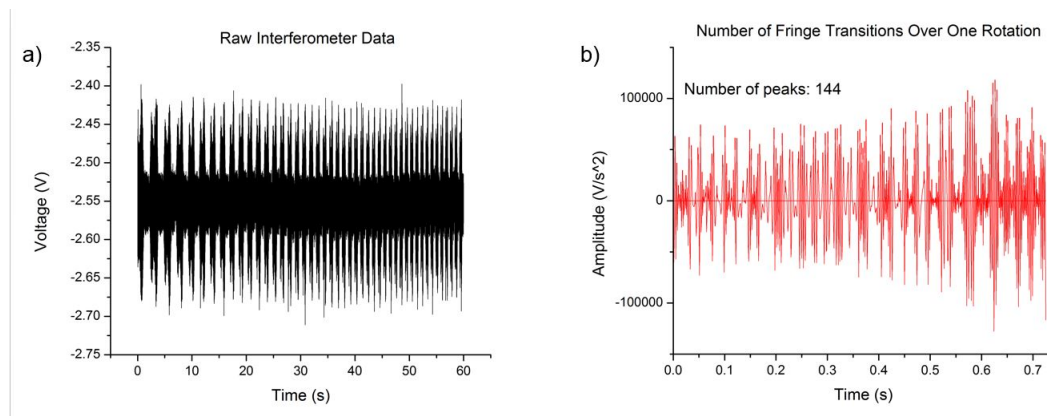


Figure 5.11: Plots show a) the raw unprocessed interferometer data taken over 60s, and features all the fringes transitioned through, and b) the processed data that features a single rotation and the fringes transitioned through in a single rotation using Origin as the software.

With the raw data, we can perform a couple of tasks. Firstly, how many fringes are transitioned through in one rotation. Taking the data and putting it through a second derivative using Origin to determine the turning points (figure 5.12 b)). Origin then allows for the ability to count the total number of waves positive waves, resulting in 144 total positive waves [16]. Taking that result and using equation 5.3 we obtain the vertical distance as $94.3 \mu\text{m}$. Leading the result of the total wobble of $\approx 2.6 \text{ mm}$. This result is logical based on the visual movement of the mass. This particular rod has a large enough TOR that it visually wobbles but is also not held by any bearings and has a single point of contact with the motor. Nevertheless, to verify we can run another test. We called this a laser bounce test, where we take a HeNe and bounce the laser off a series of mirrors up through the center feed-through and back to a quadrant photo-detector. Even with the verification method, there does need to be another test to confirm the results are in fact reasonable.

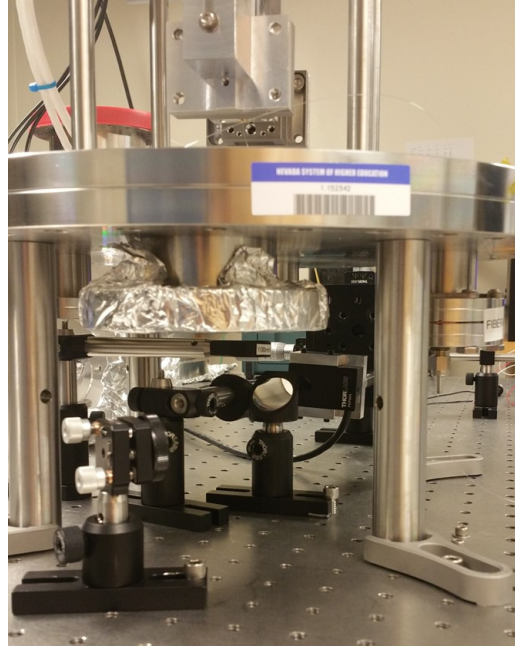


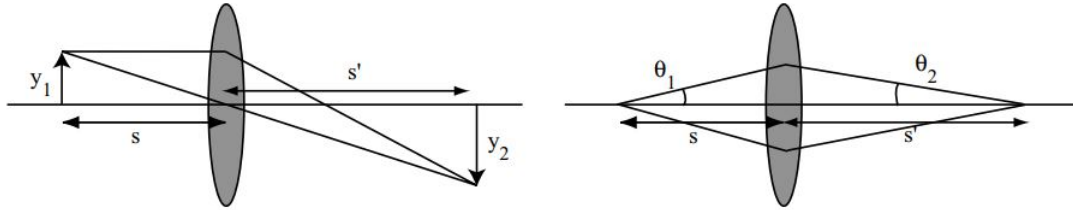
Figure 5.12: Photo of the bounce test arrangement of mirrors and photo-detector.

The primary goal of the bounce test is to collect data about the shape the rotating mirror will trace out on the detector. The shape that gets traced out is a circular shape, and thus the radius of the circle would indicate the wobble, or change in deflection. Also worth noting, the circle being traced out became too large for the detector thus a $f=100\text{mm}$ lens was used to reduce the size of the image. Once on the detector the data can be extracted via oscilloscope and plotted as the spatial dimensions of both channels. Then we can measure the radius using the following [17]:

$$y_1 = \frac{L_x(\Delta x)}{2\text{sum}} \quad (5.5)$$

Equation 5.5 describes how the photodetector measures distance. L_x is a length (mm), δx is describes by the combination of the quadrants $((B+C)-(A+D))$, and the Sum is the sum of all four quadrants. Once the radius y_1 is known then the rest of

the parameters can begin to be filled into the lens matrix. The value θ_1 is due to algebra between the radius measurement and the distance between the lens and the rotating mirror.



$$\begin{bmatrix} y_2 \\ \theta_2 \end{bmatrix} = \begin{bmatrix} 1 - \frac{s'}{f} & 0 \\ -\frac{1}{f} & 1 + \frac{s}{f} \end{bmatrix} \begin{bmatrix} y_1 \\ \theta_1 \end{bmatrix}$$

Resulting in the values for $y_2 = .741\text{mm}$ and $\theta_2 = 1.016^\circ$. Plugging into equation 5.4 we get the final result as $\approx 2.741\text{mm}$. This result is matching very close to the result from the interferometer test. Despite most of the distance measurements having to be done by hand for the bounce test, which gives us reasonable optimism for the accuracy of the interferometer tests in future iterations. Additionally, this large result is within 6 percent of the interferometer test, so due to the initial configuration, we are lead to believe the results to be reasonable for the given situation. Again, more tests need to be done to confirm.

CHAPTER 6

CONCLUSIONS AND FUTURE WORK

While there is a long road ahead of ARIADNE, that road is looking more and more clear. Through the past couple years we have made strides in verifying and developing methods for reducing magnetic fields and gradients in the sample block, and also have started on verifying those methods with the help from our collaborators. We have almost completed construction of the rotational stability chamber so that we can begin final wobble measurements with the large motor. The small motor still has work to be done concerning the spin stability. Collectively the work outlined above is providing optimism for the project. Furthermore, there is work being done by our collaborators that was not outlined above such as metrology of the sample mass, sample enclosures, and sputtering of superconductors onto various types of enclosures and measuring the shielding.

BIBLIOGRAPHY

- [1] Vassilis Anastassopoulos, S Aune, K Barth, A Belov, H Bräuninger, Giovanni Cantatore, Jose Carmona, J F. Castel, S A. Cetin, F Christensen, Jesus Collar, Theopisti Dafni, Martyn Davenport, Todd Decker, A Dermenev, K Desch, C Eleftheriadis, George Fanourakis, E Ferrer-Ribas, and K Zioutas. New cast limit on the axion-photon interaction. 05 2017.
- [2] Asimina Arvanitaki and Andrew A. Geraci. Resonantly detecting axion-mediated forces with nuclear magnetic resonance. *Phys. Rev. Lett.*, 113:161801, Oct 2014.
- [3] S. J. Asztalos, G. Carosi, C. Hagmann, D. Kinion, K. van Bibber, M. Hotz, L. J Rosenberg, G. Rybka, J. Hoskins, J. Hwang, P. Sikivie, D. B. Tanner, R. Bradley, and J. Clarke. Squid-based microwave cavity search for dark-matter axions. *Phys. Rev. Lett.*, 104:041301, Jan 2010.
- [4] R. Barbieri, C. Braggio, G. Carugno, C.S. Gallo, A. Lombardi, A. Ortolan, R. Pengo, G. Ruoso, and C.C. Speake. Searching for galactic axions through magnetized media: The quax proposal. *Physics of the Dark Universe*, 15(Supplement C):135 – 141, 2017.
- [5] S. J. Barnett. Magnetization by rotation. *Phys. Rev.*, 6:239–270, Oct 1915.
- [6] J. Beringer et al. Review of particle physics. *Phys. Rev. D*, 86:010001, Jul 2012.
- [7] Dmitry Budker, Peter W. Graham, Micah Ledbetter, Surjeet Rajendran, and Alexander O. Sushkov. Proposal for a cosmic axion spin precession experiment (casper). *Phys. Rev. X*, 4:021030, May 2014.
- [8] Saptarshi Chaudhuri, Peter W. Graham, Kent Irwin, Jeremy Mardon, Surjeet Rajendran, and Yue Zhao. Radio for hidden-photon dark matter detection. *Phys. Rev. D*, 92:075012, Oct 2015.
- [9] J.R. Claycomb and J.H. Miller. Superconducting magnetic shields for squid applications. *Review of Scientific Instruments*, 2000.
- [10] N. Crescini, C. Braggio, G. Carugno, P. Falferi, A. Ortolan, and G. Ruoso. The quax-gpgs experiment to search for monopole-dipole axion interaction. *Nuclear Instruments and Methods in Physics Research Section A: Accelerators, Spectrometers, Detectors and Associated Equipment*, 842(Supplement C):109 – 113, 2017.

- [11] Martin J. Graves Martin R. Prince Donald W. McRobbie, Elizabeth A. Moore. Mri from picture to proton. 2007.
- [12] H. Fosbinder-Elkins, J. Dargert, M. Harkness, A. A. Geraci, E. Levenson-Falk, S. Mumford, A. Kapitulnik, Y. Shin, Y. Semertzidis, and Y. H. Lee. A method for controlling the magnetic field near a superconducting boundary in the ariadne axion experiment. 2017.
- [13] Andrew Geraci, H Fosbinder-Elkins, C Lohmeyer, J Dargert, M Cunningham, M Harkness, E Levenson-Falk, S Mumford, A Kapitulnik, A Arvanitaki, I Lee, E Smith, E Wiesman, J Shortino, J C. Long, W.M Snow, C Y. Liu, Y Shin, Y Semertzidis, and Y H. Lee. Progress on the ariadne axion experiment. page 0, 10 2017.
- [14] [https://science.nasa.gov/astrophysics/focus-areas/what-is-dark energy.](https://science.nasa.gov/astrophysics/focus-areas/what-is-dark-energy)
- [15] [https://www.comsol.com.](https://www.comsol.com)
- [16] [https://www.originlab.com.](https://www.originlab.com)
- [17] [https://www.thorlabs.com/drawings/1d61165e7fa7969a_5F683A5E-D15E-AAA2-4FE5BD7251A962B5/PDP90A-Manual.pdf.](https://www.thorlabs.com/drawings/1d61165e7fa7969a_5F683A5E-D15E-AAA2-4FE5BD7251A962B5/PDP90A-Manual.pdf)
- [18] D. S. Hussey, D. R. Rich, A. S. Belov, X. Tong, H. Yang, C. Bailey, C. D. Keith, J. Hartfield, G. D. R. Hall, T. C. Black, W. M. Snow, T. R. Gentile, W. C. Chen, G. L. Jones, and E. Wildman. Polarized ^3He gas compression system using metastability-exchange optical pumping. *Review of Scientific Instruments*, 76(5):053503–053503–12, May 2005.
- [19] John David Jackson. *Classical electrodynamics*. Wiley, New York, NY, 3rd ed. edition, 1999.
- [20] Yonatan Kahn, Benjamin R. Safdi, and Jesse Thaler. Broadband and resonant approaches to axion dark matter detection. *Phys. Rev. Lett.*, 117:141801, Sep 2016.
- [21] Alexander A. Kordyuk. Magnetic levitation for hard superconductors. *Journal of Applied Physics*, 83(1):610–612, 1998.
- [22] J. E. Moody and Frank Wilczek. New macroscopic forces? *Phys. Rev. D*, 30:130–138, Jul 1984.

- [23] World Health Organization. Neutral background and human-made sources and exposure.
- [24] R. D. Peccei and Helen R. Quinn. CP conservation in the presence of pseudoparticles. *Phys. Rev. Lett.*, 38:1440–1443, Jun 1977.
- [25] R. H. Romer. Nuclear spin relaxation in liquid he^3 ii. *Phys. Rev.*, 117:1183–1187, Mar 1960.
- [26] M. Tejedor, H. Rubio, L. Elbaile, and R. Iglesias. External fields created by uniformly magnetized ellipsoids and spheroids. *IEEE Transactions on Magnetics*, 31(1):830–836, Jan 1995.
- [27] Steven Weinberg. A new light boson? *Phys. Rev. Lett.*, 40:223–226, Jan 1978.
- [28] F. Wilczek. Problem of strong p and t invariance in the presence of instantons. *Phys. Rev. Lett.*, 40:279–282, Jan 1978.